FACULTY
OF MATHEMATICS
AND PHYSICS
Charles University

BACHELOR THESIS

Jakub Maruška

Tuning the crystal growth condition of Ni50Mn28.5Ga21.5 magnetic shape memory alloy

Department of Condensed Matter Physics

Supervisor of the bachelor thesis: RNDr. Klára Uhlířová, Ph.D.

Study programme: Physics

Specialization: General Physics

Prague 2019

I declare that I carried out this bachelor thesis independently, and only with the cited sources, literature and other professional sources.

I understand that my work relates to the rights and obligations under the Act No. 121/2000 Coll., the Copyright Act, as amended, in particular the fact that the Charles University has the right to conclude a license agreement on the use of this work as a school work pursuant to Section 60 paragraph 1 of the Copyright Act.

In…..... date..... signature

I would like to thank the supervisor of my thesis RNDr. Klára Uhlířová, Ph.D., for her contagious enthusiasm for physics, invaluable feedback and the time she dedicated to helping me. Furthermore I am very thankful to my consultant Ross Harvey Colman, Dr. for insightful consultations, literature recommendations, help and supervision during the measurements and a friendly workplace atmosphere he creates.

Also I want to thank RNDr. Milan Klicpera, Ph.D. for his assistence with sample preparation. I am grateful to Ing. Barbora Vondráčková, RNDr. Marie Hrůzová Kratochvílová, Ph.D. for the DSC and dilatometry data they provided.

Lastly I would like to thank my friends and family for their support and encouragement throughout my studies and most importantly exam periods.

Title: Tuning the crystal growth condition of Ni50Mn28.5Ga21.5 magnetic shape memory alloy

Author: Jakub Maruška

Department: Department of Condensed Matter Physics

Supervisor of the bachelor thesis: RNDr. Klára Uhlířová, Ph.D., Department of Condensed Matter Physics

Abstract: Ni_2MnGa as representative of magnetic memory shape alloys is gaining popularity in recent years as promising smart material. Most interesting phenomena are observable in single crystals near the martensitic transition temperatures. The strong dependence of its properties on composition is very important for future applications. In order to study its properties, good single crystal with room temperature martensitic transition is desirable. This thesis is focused on tuning growth of crystal in optical floating zone furnace and measuring transition temperatures. To that end multiple specimen with different composition were prepared and their composition and crystalline structure studied by EDS and Laue diffraction. Transitions were studied by magnetisation, calorimetry and dilatometry measurements.

Keywords: MSM, Martensitic transition, Heusler alloys

Introduction

In 1903 Friedrich Heusler first showed that alloy Cu_2MnAl is ferromagnetic despite none of the elements are ferromagnetic by themselves. This alloy represents group ternary intermetallics with a 2:1:1 stoichiometry and $L2_1$ crystalline structure called Heusler alloys. They display many interesting behaviours and properties, for example: Magnetocaloric effect (MCE), Superelasticity (Pseudoelasticity) and Magnetic shape memory (MSM). Besides that these compounds are extraordinary in their ability to be physically tuned, which suggest possibility of new properties with great application potential, for example in spintronics and energetics (i.e. Refrigeration) [1,3].

Magnetic shape memory is name for different effects which produce magnetic field induced strain. One promising example of MSM alloys is Ni_2MnGa, which was observed to deform up to 12% in homogenous magnetic field. MSM effects are closely related to martensitic transition occurring for Ni_2MnGa at roughly 200K. As stated before properties of this alloy can be tuned, for example temperature of martensitic transformation and Curie temperature can be manipulated by changing composition [3]. It is desirable to study properties of Ni_2MnGa as single crystals, because of their application potential as actuators (martensitic transformation) [4].

This thesis is focused on testing optical floating zone furnace for growing single crystals of $Ni_{50}Mn_{28.5+x}Ga_{21.5-x}$ with $x \in (0,2)$. Optical floating zone furnaces are usually used for growing non-metallic compounds with much higher melting points and lower vapour pressures than our material. In the course of this work, four samples were prepared and studied for homogeneity and single crystal quality (presence of grains). On selected samples further measurements (dilatometry, calorimetry and magnetization) were conducted.

The first and second chapters attempt to explain important concepts and phenomena, familiarize reader with nomenclature and describe used equipment and its functionality. In the third chapter used preparation technique and its improvements are discussed. The fourth chapter contains characterisation of prepared samples, measured data and discussion. The last chapter summarises and attempts to draw conclusions.

1. Theory

1.1. Phase transition

A phase is defined as a region of space in which all physical properties are homogeneous and is separated by boundary, where properties change discontinuously. Phase transition is a process during which system changes some of its physical properties in response to change in outside conditions. Most commonly known phase transitions are changes between states of mater (i.e. solid-liquid…) Ehrenfest postulated phase transition categorisation according to changes of derivative of Gibbs potential.

First-Order phase transitions are those that have discontinuity in first derivative of Gibbs potential, with respect to some thermodynamic variable. Example of such transition can be structural change of crystal lattice accompanied by exchange of latent heat, which involves jump in entropy.

Second-order phase transitions have discontinuity in second derivative of Gibbs potential, while being continuous in first derivative. These can be discontinuous change of heat capacity or magnetic ordering without change of structure. By analogy there could be higher order transitions, but these were never observed [5].

Phase of system is dependent on outside thermodynamic parameters. In Figure 1 composition phase diagram for nickel manganese alloy is presented. There is liquid phase for high temperatures or high gallium composition, and many more phases with different ordering in solid state. Constructing such diagrams, with more degrees of freedom is increasingly difficult and requires a lot of experimental measurements.

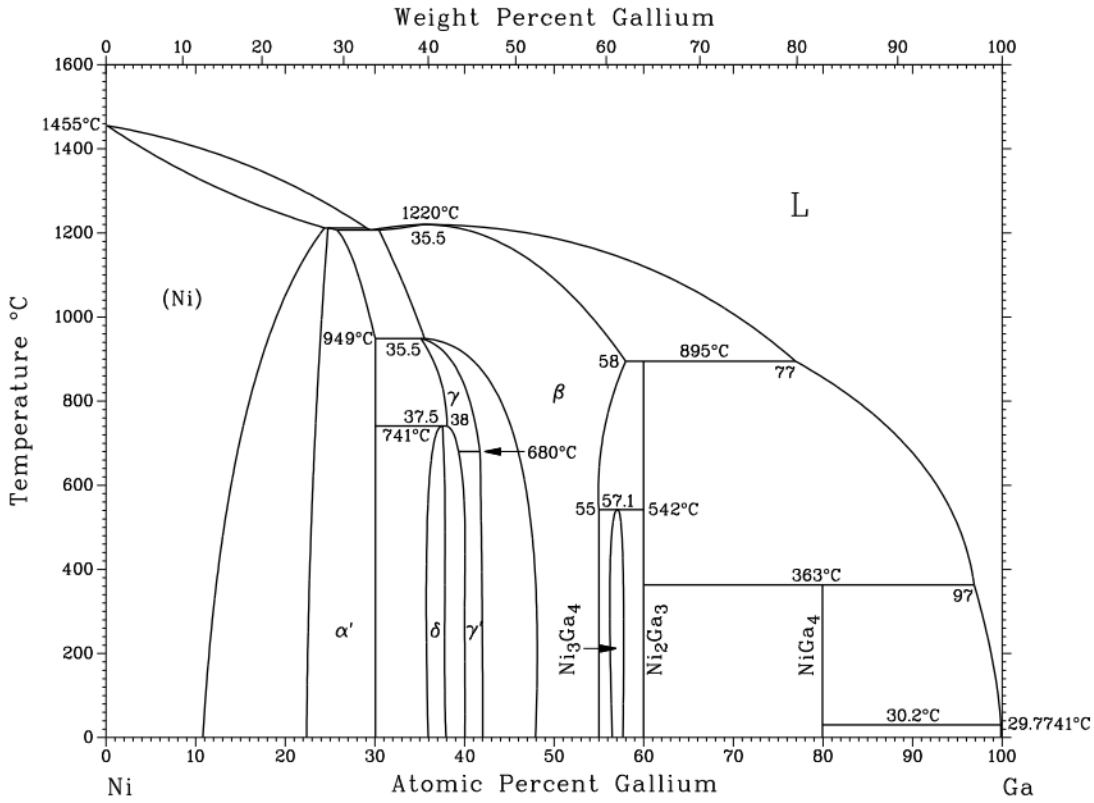

Figure 1 - Phase diagram for Ni-Ga binary system, showing many different possible phases within solid state dependent on temperature and composition (from Ref. [6]*).*

1.1.1. Composition dependence of the phase transitions

Composition of a crystal grown using zone melting technique differs from parent rod. As the liquid molten material cools down and solidifies it passes through the liquid solid coexistence phase (see Figure 2). At temperature T the liquid has different concentration from solid phase, which results in composition discrepancy between parent rod and grown crystal. When the molten zone is slowly moved along the rod it produces concentration dependency on position:

$$c_s = c_0 \left[1 - (1-k)\, exp\left(-\frac{k}{l}x\right)\right] \quad (1)$$

where c_s is concertation at point x, c_0 is concentration in the parent rod, k is distribution coefficient, l is length of the zone and x is position on the rod from the beginning of melting [7, 8]. The composition gradient is plotted in Figure 3, for rod length 90 mm, zone length 6 mm and k equal 0.88. At the beginning the concentration is lower than parent, but it approaches parent composition and stabilises. After some length the zonal method produces uniform concentration.

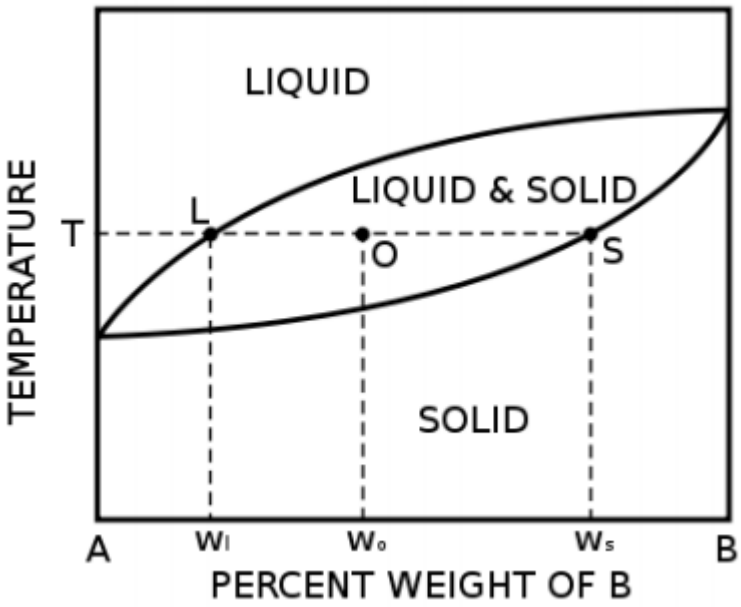

Figure 2 – Schematic binary phase diagram, illustrating composition change during solidification of alloy (from Ref. [8]*). W_s is concentration in solid phase, W_l is concertation in liquid phase and W_o of liquid-solid mixture.*

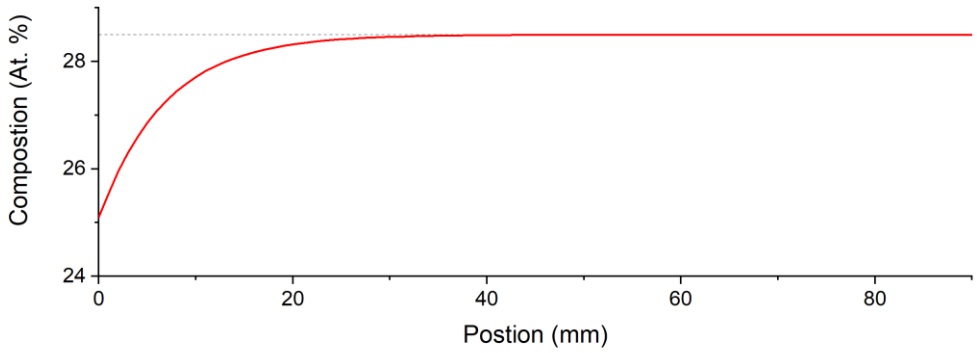

Figure 3 - Theoretical composition along rod for binary alloy from equation (1)*, for l = 6mm and k = 0.88.*

1.1.2. Martensitic transition

Martensitic phase transition is a transformation from a cubic (austenite) phase to a low symmetry phase (martensite, see Figure 4). It is a first order diffusionless transformation in solid state. The transition is called martensitic when changing from austenite to martensite and austenitic when changing to austenite. Martensite phase is monoclinic with magnetic easy axis along shorter c_M crystallographic vector, maximal strain produced by this transition is dependent on the unit cell dimensions, in this case theoretical strain is $\varepsilon_0 = \frac{a_M - c_M}{a_M}$ (subscript denotes that dimensions are for

martensitic phase). The transition occurs via small and cooperative movement of many atoms. These small movements require very little energy therefore this transition doesn't require much energy and takes place at fairly low temperature, for Ni_2MnGa alloy it is ~200K, but for materials studied here it can start above room temperature at roughly ~300K. During phase transition, interfaces between parent phase and growing phase emerge, any incompatibility is accompanied by formation of twin structures [9].

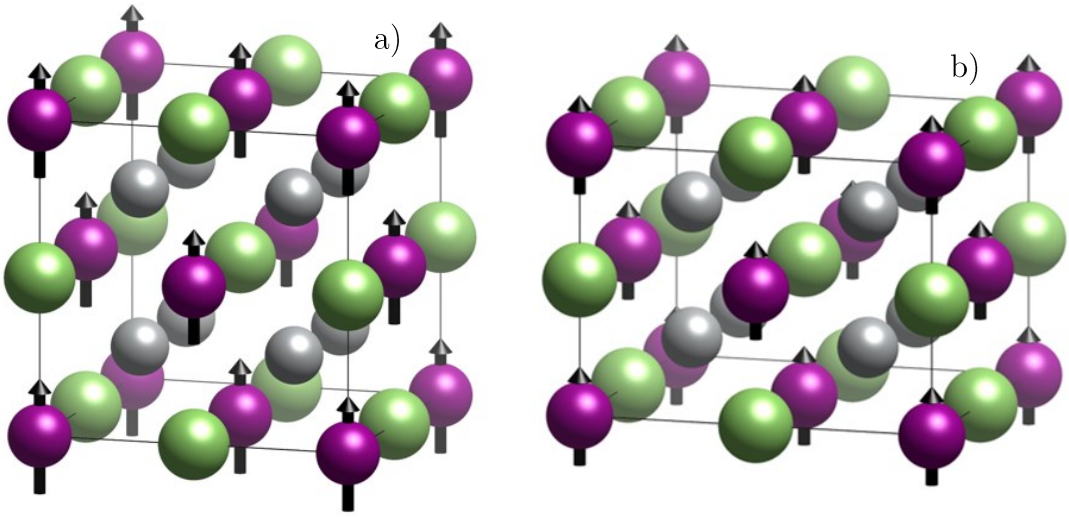

Figure 4 - Comparison of austenite (a) and martensite (b) phase. Where grey represents Ni atoms, purple Mn atoms and green Ga atoms. Arrows represent magnetic moments (from Ref. [10]*).*

1.2. Magnetic Properties

Basic categories of magnetic behaviours are: diamagnetism, paramagnetism, ferromagnetism, antiferromagnetism and ferrimagnetism. Type of dominant magnetic behaviour can be determined by the response of material to external magnetic field. Main characteristics are temperature dependence of magnetization (M) and magnetic susceptibility (χ). In general, magnetic susceptibility is defined as:

$$\chi = \left(\frac{dM}{dH}\right)_T, \tag{2}$$

where M is magnetization of material and H is external magnetic field [5, 11].The materials studied here are either in paramagnetic or ferromagnetic phase.

1.2.1. Paramagnetism

Paramagnetism is a type of magnetic behaviour seen in many materials, namely in austenite phase of Ni_2MnGa. In paramagnetic materials, the exchange interactions

between present magnetic moments are so weak that there is no magnetic ordering. Magnetization is approximately linearly dependent on applied magnetic field, using the equation (2) we get:

$$M = \chi H.$$

The temperature dependence of magnetic susceptibility of paramagnets obeys Curie law:

$$\chi = \frac{C}{T}\,, \tag{3}$$

where C represents constant that is proportional to the sum of squares of effective magnetic moments in unit volume. Constant C is called Curie constant [11, 12].

1.2.2. Ferromagnetism

In martensitic phase, ferromagnetic behaviour can be observed in Ni_2MnGa. Ferromagnetism is a type of magnetic ordering, with magnetic moments in the materials oriented parallel to each other. In ferromagnets, the exchange interaction between the magnetic moments results in their parallel order. However, in non-magnetized state, the materials are composed of many differently oriented domains in order to minimize magnetostatic energy. This in sum gives zero macroscopic magnetization. The magnetization process is described in Figure 5: Assuming the external magnetic field is applied parallel to the easy magnetization direction, the domains with magnetization oriented parallel to the external magnetic field grow at the expense of the other domains, reaching saturation at H_s. The first magnetization curve starting from non-magnetized state is called virgin curve. When releasing the magnetic field, the magnetization doesn't decline along the virgin curve. At zero magnetic field, the samples has non-zero remanent magnetization M_r. To obtain zero magnetization, coercive field H_c (a field with opposite direction to that of the field which previously magnetized the sample) is needed. This state is unstable. When the field is removed, magnetization of the sample becomes non-zero again (not shown in the figure). Continuing with magnetization to higher negative magnetic field, - M_s is reached. The loop is then symmetric with respect to applied magnetic field.

Magnetic hysteresis is prominent feature of ferromagnets. From that it can be seen that current magnetization of ferromagnet is determined by its magnetization history.

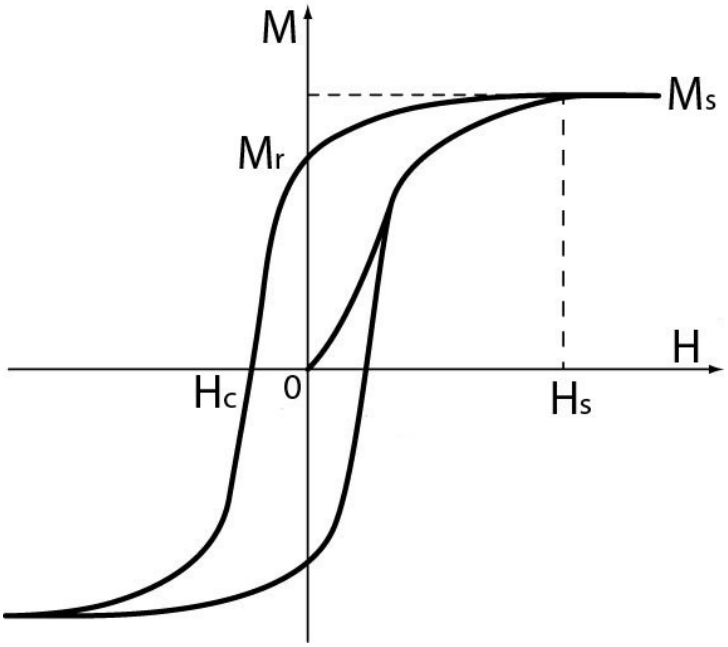

Figure 5 - Theoretical hysteresis loop of ferromagnet, where H_s is saturation field with saturation magnetization M_s, M_r is remanent magnetization and H_c is coercive field (from Ref. [13]*).*

At Curie temperature, usually denoted T_C, ferromagnetic order vanishes. At temperatures significantly higher than the Curie temperature they start to behave like paramagnets and their susceptibility according to Curie-Weiss law is:

$$\chi = \frac{C}{T - \Theta_p}. \tag{4}$$

The parameter Θ_p is called the paramagnetic Curie temperature [11, 12].

1.2.3. Magnetically induced phase transition

Up till now we discussed influence of temperature on martensitic transition, but since main feature of MSM alloys is their multiferroic behaviour, this also can play role in martensitic transformation. Martensitic transformation can be induced by magnetic field as well, in analogy with memory shape alloys where mechanical stress takes the role of magnetic field. However to produce this transformation, powerful magnets are required. Underlying mechanism can be explained by magnetization

difference between phases. When magnetic field is applied structure changes to one with higher magnetization in order to lower its magnetic energy.

When sample is transformed into martensite it's called magnetically induced martensite (MIM) and when it's transformed into austenite it's called magnetically induced austenite (MIA). Still technological limitations make this possible only for samples at temperatures close to those of thermal martensitic transition and therefore the field essentially changes the transformation temperature. Due to the differences in unit cell dimensions, the unit cell is elongated in one direction, while shortened in other two. This can produce macroscopic deformation, which is reversible, provided that the width of thermal hysteresis is small [9].

1.2.4. Magnetically induced reorientation

Magnetically induced reorientation (MIR) takes place within one phase and for this effect to produce any strain, the unit cell cannot be cubic. Material in magnetic field tries to lower its magnetic energy, therefore in case that sample is not oriented along easy axis, different variants will emerge creating twin boundaries between them. Due to relatively easy twin movement correctly oriented variants will grow via movement of twin boundaries with increasing magnetic field. Ultimately this leads to a single variant crystal oriented in the same direction as magnetic field. Once again a parallel between physical stress and stress induced by magnetic field can be drawn at this point. Stress-strain curve is similar to that of reorientation induced by physical force.

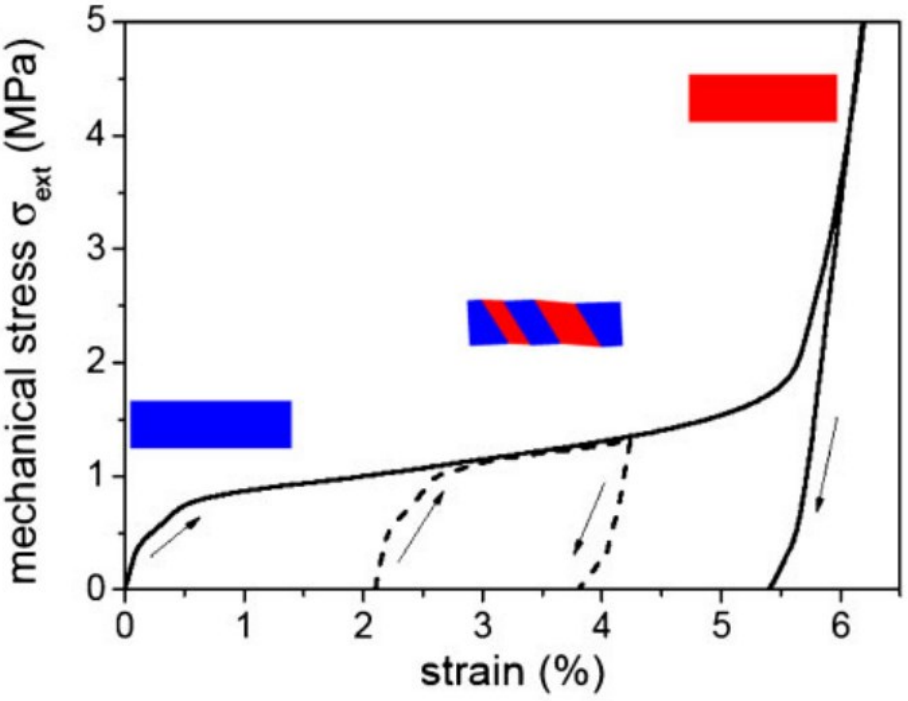

Figure 6 - Strain vs Stress in memory shape alloy(from Ref. [9]*).*

Figure 6 shows stress-strain curve, initially higher increase in stress is required to induce strain, but after reaching activation barrier, deformation is easier. In single variant crystal it is because energy is needed to nucleate new variants and create twin boundaries. This initial jump is observed even in already twinned materials that may be caused by other mechanisms such as need to unpin existing boundaries or create new boundaries with higher mobility. To completely reorient crystal, much higher field is necessary [9].

2. Methods

2.1. Scanning electron microscopy (SEM)

Scanning electron microscope is an imaging device that uses focused electron beam to scan surface of samples. Schematic illustration of inner components of SEM is presented in Figure 7. The electrons, which are provided by electron gun, are accelerated to high energy (up to 40 keV) and focused by magnetic lenses. The electrons interact with sample, causing emission of photons and electrons which are detected by various detectors.

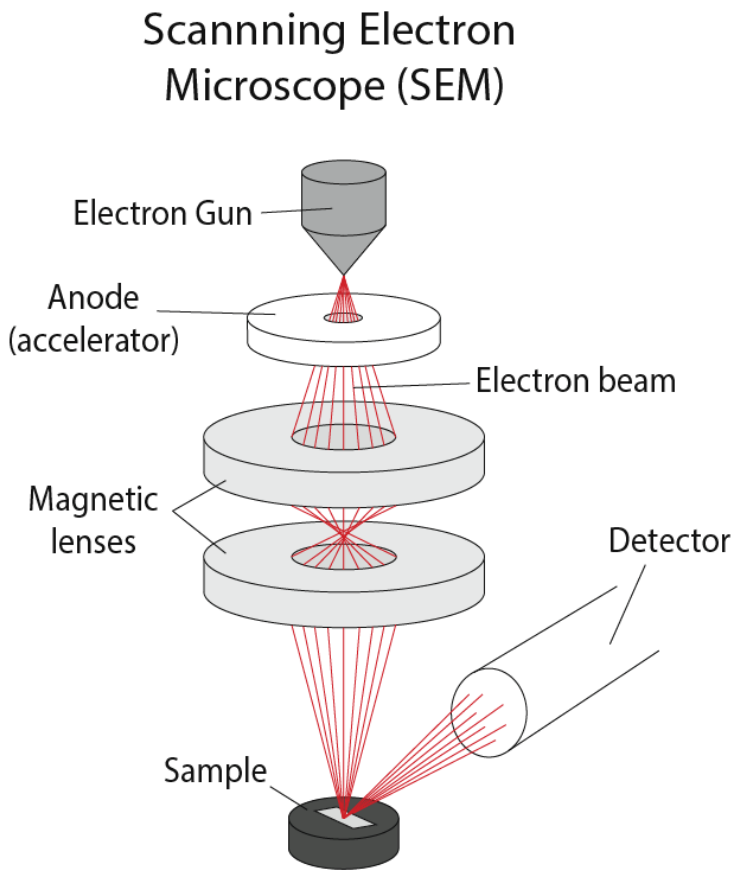

Figure 7 - Schematic view of SEM. Electron gun provides electrons which are then accelerated by anode and then focused by magnetic lenses. Beam hits sample and causes various emissions which are measured by detector (from Ref. [14]*).*

Upon inelastic scattering of primary electrons (PE), secondary electrons (SE) are emitted. SE provide information about surface features of scanned sample. Primary electrons that are scattered elastically, back scattered electrons (BSE) are reflected directly back and are detected by detector situated around the final aperture of

magnetic optics. With growing atomic number, the cross section of the elastic scattering increase. Therefore the BSE provide composition contrast [15].

X-rays are produced two ways by PE interacting with sample. First way is when electron is decelerated by sample and energy of electron is carried off as bremsstrahlung. Bremsstrahlung is continuous spectrum that needs to be discounted in further analysis. Second way is when an electron is removed from the inner shell of atom, the vacancy is filled by an electron from a higher shell accompanied by emission of photon with energy associated with atomic electron transition. This energies constitute characteristic spectrum of atom. The spectral lines are denoted by primary quantum numbers of the shells as $N_{m\text{-}N}$ where N identifies inner shell (K, L, M…) and the second outer shell. The second number is given as corresponding letter of Greek alphabet, for example peak K_{β} means that electron from shell M filled vacancy in shell K [16]. Example of EDS spectrum is shown in Figure 8, where K series are highlighted for nickel. At lower energies, there are three L series spectral lines.

Energy dispersive x-ray spectroscopy (EDS) uses this to examine composition of material. Based on comparison of intensity of peaks in sample to pure elements and using the so called ZAF corrections ("Z" for atomic number, “A” for absorption and “F” for fluorescence corrections) content of each element is calculated.

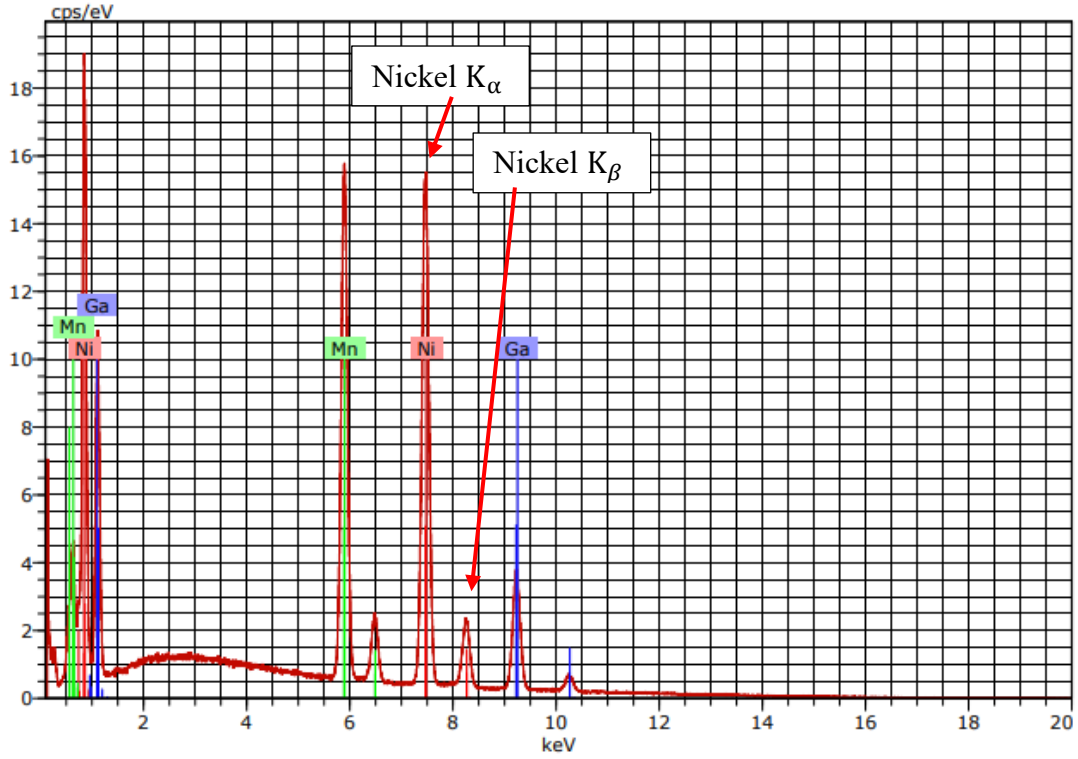

Figure 8 - EDS spectrum of rod R28a taken along axis of growth.

Microscope TESCAN Mira I LMH with Bruker AXS Quantax detector was used for all EDS data acquisition. For all readings working distance 16,5mm, magnification 500x and spot of size 56.6x56.6µm was used.

2.2. Laue Diffraction

To determine quality and orientation of the crystals, Laue X-ray diffractometer Photonic Science was used. Back-Reflection Laue diffraction uses multispectral X-ray beam, which is diffracted by the studied sample onto a detector (see Figure 9). The positions of maxima on the detector are given by Bragg's law:

$$2d_{hkl}\,sin(\alpha) = \lambda, \tag{5}$$

where α is angle between incident beam and diffracted beam and d_{hkl} are crystallographic plane distances. The Laue pattern symmetry can be used to identify crystallographic orientation of the sample. In Figure 9 is an example of Laue diffraction pattern, with incident beam along a four-fold axis [17].

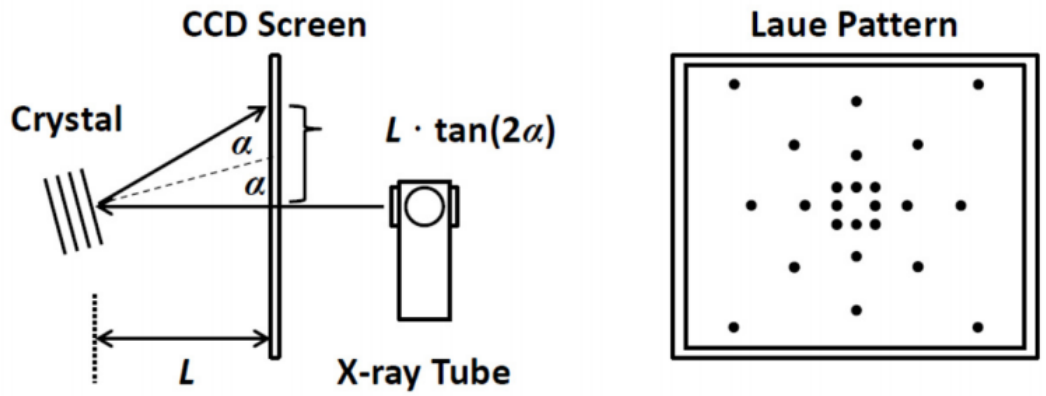

Figure 9 - Schematic representation of Back-Reflective Laue Diffraction (from Ref. [18]*).*

2.3. Magnetization measurements

Magnetization data was measured using Vibrating-sample magnetometer (VSM) in Physical Property Measurement System (PPMS) or SQUID magnetometer in Magnetic Property Measurement device (MPMS). The PPMS allows measurements of various properties, in wide range of temperatures and magnetic fields.

The sample attached to a glass holder by teflon tape or fixed in PE straw is inserted inside the apparatus. The sample is magnetised in a uniform magnetic field and then vibrated. Induced voltage is measured and magnetization is determined by Faraday induction law. This way magnetization can be measured in wide temperature range to identify magnetic transitions in material [19].

2.4. Differential scanning calorimetry

Differential scanning calorimetry (DSC) was measured using SETSYS Evolution TGA-DTA/DSC SETARAM. DSC is a method that measures difference in the amount of heat required to increase temperature of a sample and a reference. With known heat capacity of the reference, the heat capacity of the sample can be determined. This method is useful for identifying martensitic and austenitic transitions, because as first order transitions, they transfer latent heat. The change of heat capacity at Curie temperature is visible too.

2.5. Dilatometry

Using dilatometers, temperature dependence of thermal expansion was measured. The sample is placed in a sample holder, touching holder on one side and a push rod on the other. Constant force is applied at the sample and any length change caused by temperature change is transferred by the push rod onto measuring system. Because martensitic transition is a first order structural transition and structure changes from cubic to monoclinic, it can be identified by sudden deformation [20].

3. Sample preparation

All samples were prepared from elements of the same respective purity and using the same set of equipment. Material for preparation was weighted with difference from target weight no more than 100 μg. It was then melted to produce polycrystalline rod and melted again in floating zone furnace.

3.1. Used elements

Purities of elements were as follows: nickel slug 4N, manganese pieces 3N and gallium ingot 6N. Nickel and gallium were used as they were purchased, while manganese was cleaned due to surface contamination with oxides. Although manganese is supplied in glass container sealed in argon atmosphere that prevents it from oxidizing, the pieces were dark brown suggesting surface oxidation. In this instance it was cleaned with roughly 10% solution of nitric acid and used right after weighting to minimise oxidation after cleaning.

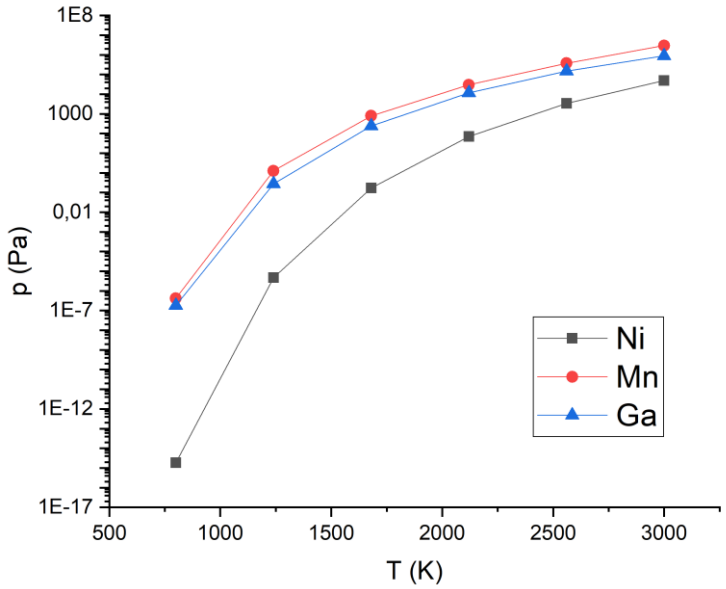

Figure 10 – Ratio of tension of vapour between nickel and remaining elements.

A significant factor, which influences the composition of our alloys is evaporation of elements during melting. Even though there is no exact known relation between vapour pressure and rate of evaporation, it is good indicator of which element evaporates more. Figure 10 shows vapour pressure of all used elements. It can be seen

that Mn and Ga have significantly higher vapour pressure than nickel. Because of that when preparing samples more of both manganese and gallium was added to offset this suspected evaporation.

For all weighting, balance Sartorius CPA225D-0CE was used. It is a highly precise balance with accuracy class I [21], resting on anti-vibration table. First nickel was weighted, aiming at half of target weight, split into four evenly big groups. Based on actual mass of nickel, target weights of rest of the elements were calculated.

3.2. Arc-melting

The elements were melted together using a Monoarc furnace (custom made by Vakuum Praha and Dicont). It is device that uses electrical arc to melt material (see Figure 11). It consists of water cooled, copper, removable crucible and movable tungsten electrode enclosed in vacuum chamber. The chamber is pumped to 10^{-4} Pa. and then backfilled with argon just prior to melting. Two types of crucibles were used, the first one with four circular cavities for melting the elements into alloy and the second one with two rod like cavities for rod preparation.

The prepared elements were first placed into the crucible with circular cavities and melted. After first melting a pellet was formed, which was then flipped and melted again. This process was repeated for each pellet three times. Then the pellets were cleaned and broken into smaller pieces that would fit into the second crucible. The material was then again melted to produce rod (see Figure 12). All melting was done as evenly and as fast as possible to prevent inhomogeneity and excessive evaporation of material.

During melting some material evaporated, which was evident from deposits of black substance on inner surfaces of crucible and chamber, the products were also weighted to monitor the mass losses.

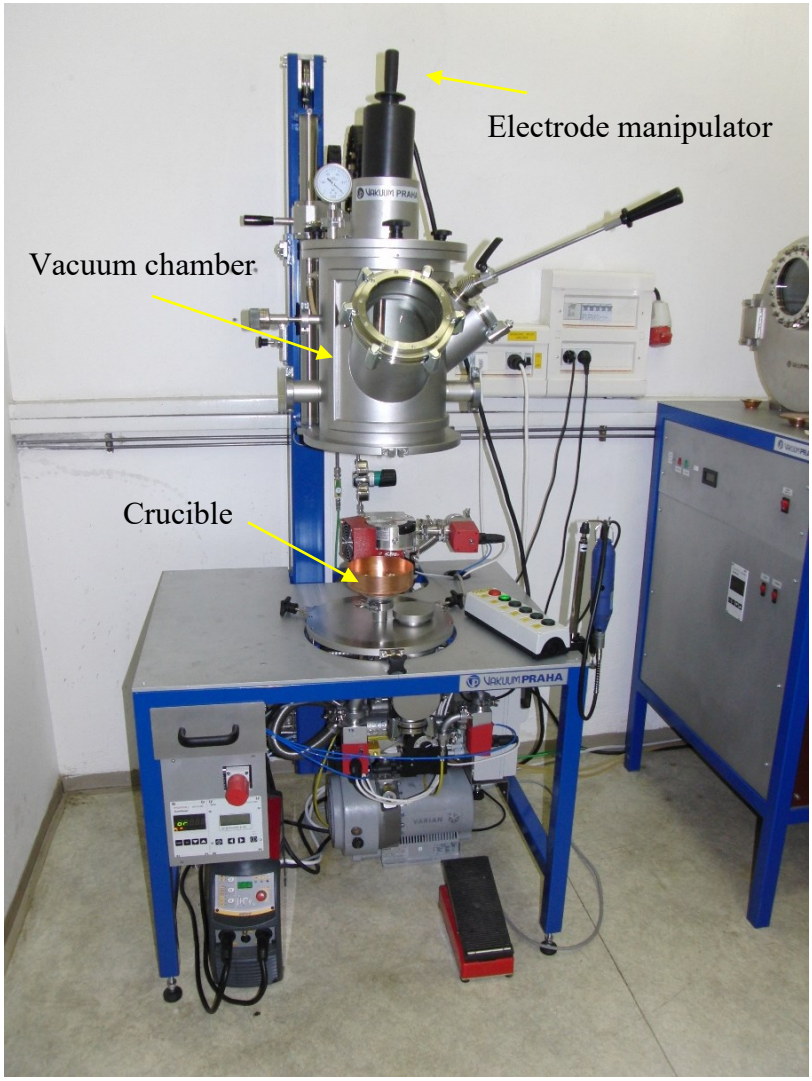

Figure 11 - Monoarc, device used to prepare polycrystaline samples and rods, using electrical arc for melting.

Figure 12 - Polycrystalline rod R29,5 prepared by monoarc.

3.3. Floating zone furnace

For the crystal growth, a floating zone furnace FZ-T-4000-VI-VPM-PC by Crystal Systems Corp was used. It consists of four xenon lamps, four ellipsoidal mirrors arranged as in Figure 13 a), pulling mechanism and gas distribution system with vacuum tight quartz tube serving as a sample environment (vacuum or gas atmosphere). The mirrors focus light from the lamps at small area on rod, heating it to

high temperature. The temperature (melting point) is estimated visually using camera and regulated by changing power to the lamps.

The rod itself is attached to a puling mechanism and placed in the quartz tube. In our case, argon protective atmosphere was used. The tube was first pumped, then backfilled with argon (6N purity) that was continuously flowing through the tube to prevent deposition on the quartz tube obscuring lamps. The pressure inside the quartz tube was 4.10^5 Pa with flow rate 0.25 l/min.

For construction reasons, the rod needs to be cut into two pieces that are then mounted on the pulling holders. At the beginning, these two pieces are brought adjacent to each other and slowly heated up, until their ends melt and can be joined, which can be seen in Figure 13 b). After that the rod is slowly moved through the hot zone enabling formation and growth of crystals.

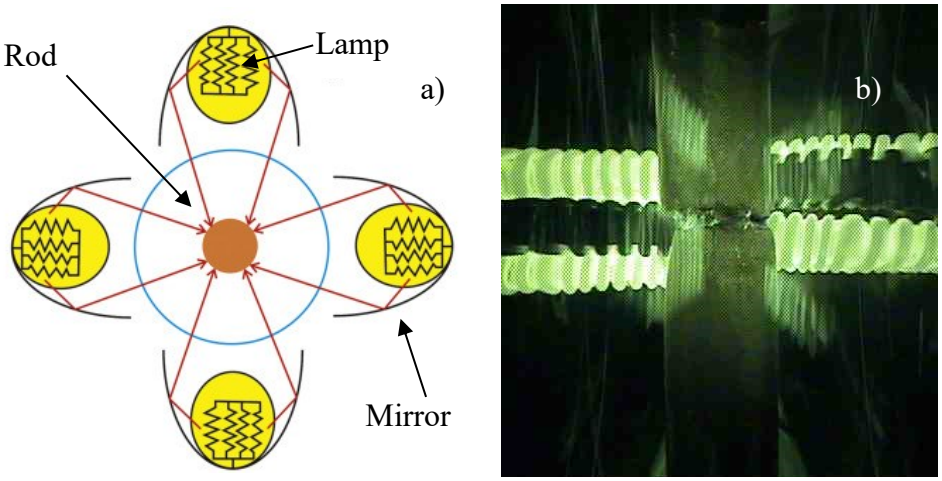

Figure 13 - a) Schematic of inner chamber of floating zone furnace (from Ref. [22]*), b) inner view of floating zone furnace just after joining of rod.*

Despite the used argon flow, some material was deposited on the quartz tube during each growth, indicating that once again material evaporated, presumably manganese and gallium.

3.4. Annealing

In order to improve homogeneity and crystalline structure, annealing was used, all rods were annealed prior to measurements. The samples were sealed in quartz tubes under protective argon atmosphere and heated up at rate 5°C per minute to 1000°C. They were left at this temperature for 48 hours, then cooled down to 800°C and

annealed for 48 hours more. Following that they were cooled down to room temperature slowly at rate 0.5°C per minute. Annealed sample R29.5 is shown in Figure 14. It has one side polished, for EDS analysis. Approximately in the middle of the sample, possible twin boundaries are noticeable as area with slightly different reflectivity.

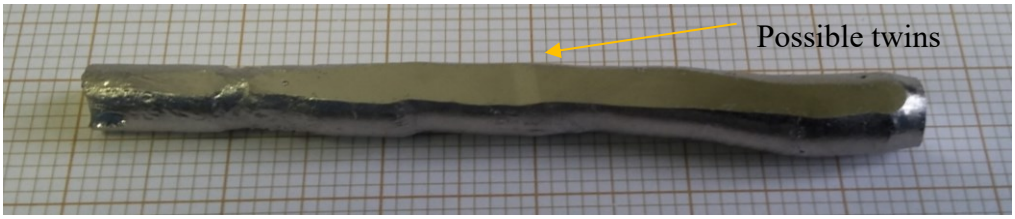

Figure 14 - Annealed rod R29.5 with polished side, showing signs of possible twins at surface.

4. Results

4.1. Prepared samples

Using the methods described above, four rods with different stoichiometry were prepared. Rods will be denoted according to their target manganese content R(Mn atomic percentage).

4.1.1. Composition

Rods R28a and R28b were prepared first with fairly similar stoichiometry. Based on vapour pressure of constituent elements, loss of manganese and gallium was expected greater than that of nickel, therefore 3% more manganese and 3% more gallium was added into sample precursor to compensate for loss during melting.

Table 1 - Target stoichiometry for all rods and their preparation parameters.

Name	Stoichiometry	Growth speed	Excess Mn	Excess Ga
R28a	$Ni_{50}Mn_{28}Ga_{22}$	$5mm.h^{-1}$	3%	3%
R28b	$Ni_{50}Mn_{28,5}Ga_{21,5}$	$2mm.h^{-1}$	3%	3%
R29.5	$Ni_{50}Mn_{29,5}Ga_{20,5}$	$2mm.h^{-1}$	6%	3%
R30.5	$Ni_{50}Mn_{30,5}Ga_{19,5}$	$2mm.h^{-1}$	6%	3%

After the samples were prepared, EDS was conducted to assess homogeneity and determine actual composition of each rod. Before measuring composition, ends of rods, which were not melted by the floating zone furnace, were removed. All rods were polished along the axis of growth and multiple readings were taken from this surface. The compositions of rods R28a and R28b are depicted in Figure 15 and Figure 16, respectively. As can be seen, both rods are nickel rich and demonstrate significant variation of composition along axis of growth, Y defines the distance from the beginning of the growth.

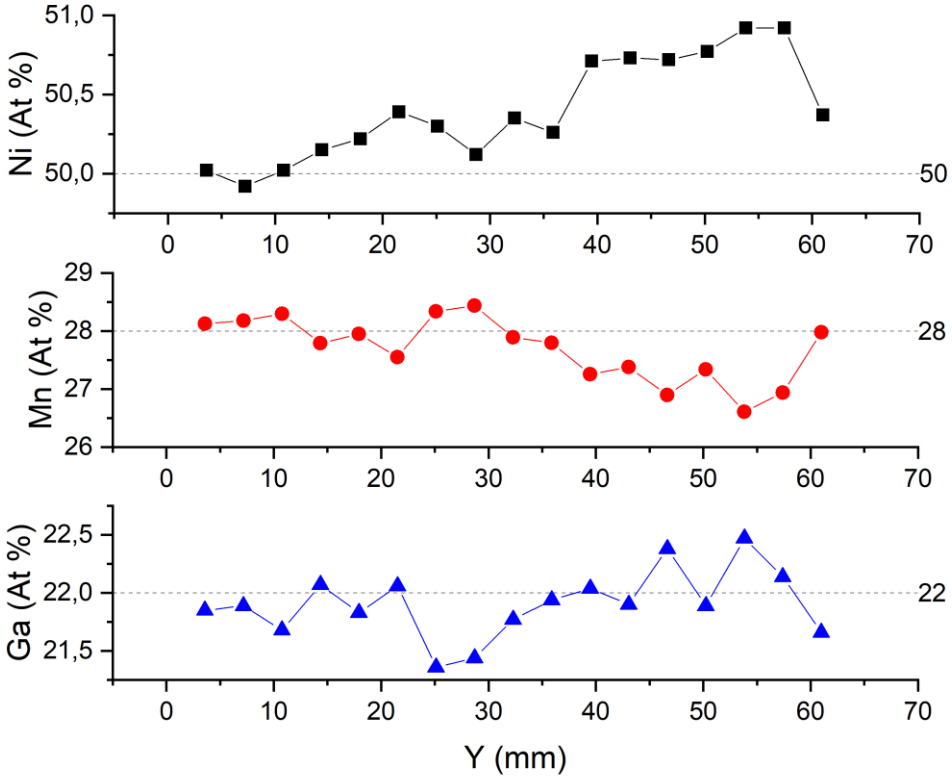

Figure 15 - Composition of rod R28a along axis of growth. The dashed lines show the target composition.

One cause of the nickel excess may have been oxidisation of the other two elements during melting. After the arc melting into pellets and the precursor rod, green coloration on surface was observed. This coloration is most likely result of oxidation of one (or more) of the constituting elements. Two possible green oxides come into consideration, NiO and MnO. Nickel oxide is produced upon heating of nickel above 400°C which is achieved during melting. This might lower the nickel content resulting in nickel deficient rod. However excess of nickel in resulting rod indicates that this is not the case, or that this effect impacts composition to a lesser degree than loss of the

other two elements.

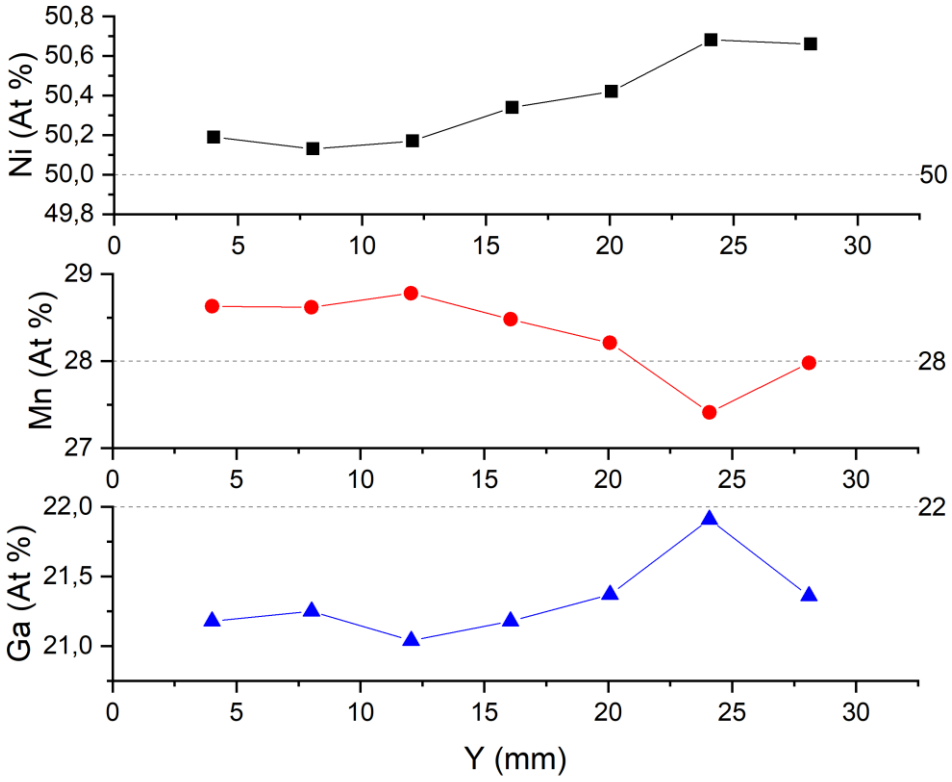

Figure 16 - Composition of rod R28b along axis of growth. The dashed lines show the target composition.

Manganese on the other hand is very reactive in its pure form, which was observed during preparation, as it started to react with air very quickly. It is possible that manganese oxides were introduced in to the rods during sample preparation. To avoid further contamination of the samples, the surface was polished by sandpaper prior all further meltings (this however possibly means that more manganese has been removed during preparation). Therefore, in the other prepared rods R29.5 and R30.5 more manganese (+6%) was added to substitute nickel. This raised manganese content, which can be seen in Figure 18 and in turn lowered resulting nickel content as anticipated, which can be seen in Figure 17. It was expected that manganese would substitute nickel. However as can be seen in Figure 19 this was not entirely correct and adding more gallium is required to better match target composition.

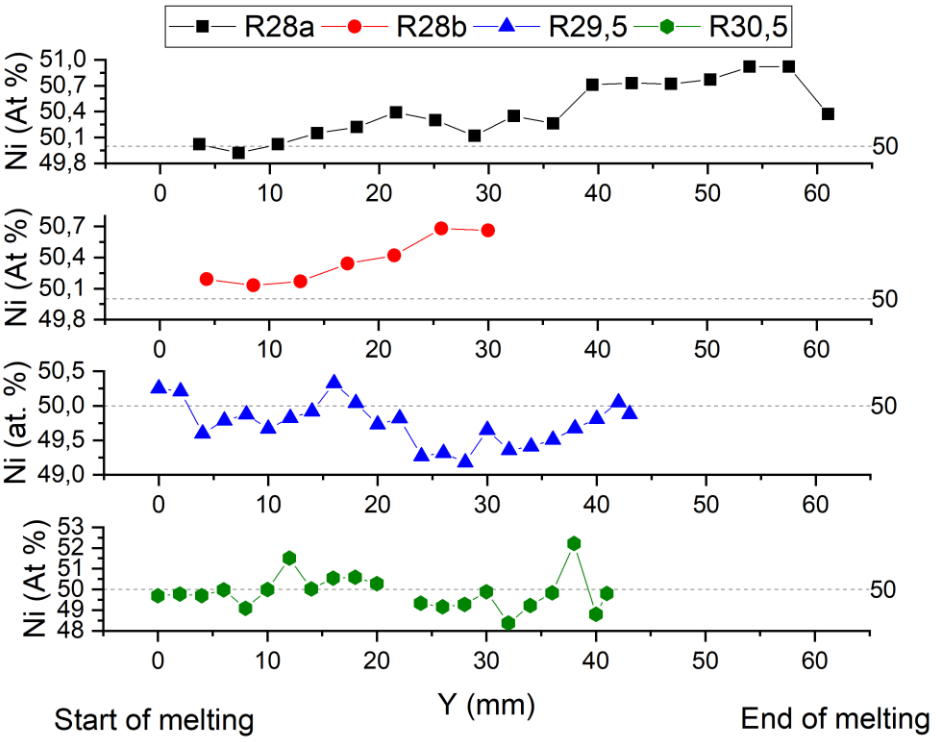

Figure 17 - Nickel composition of all prepared rods along axis of growth, with dashed line representing target composition. Y is the distance from the beginning of the growth.

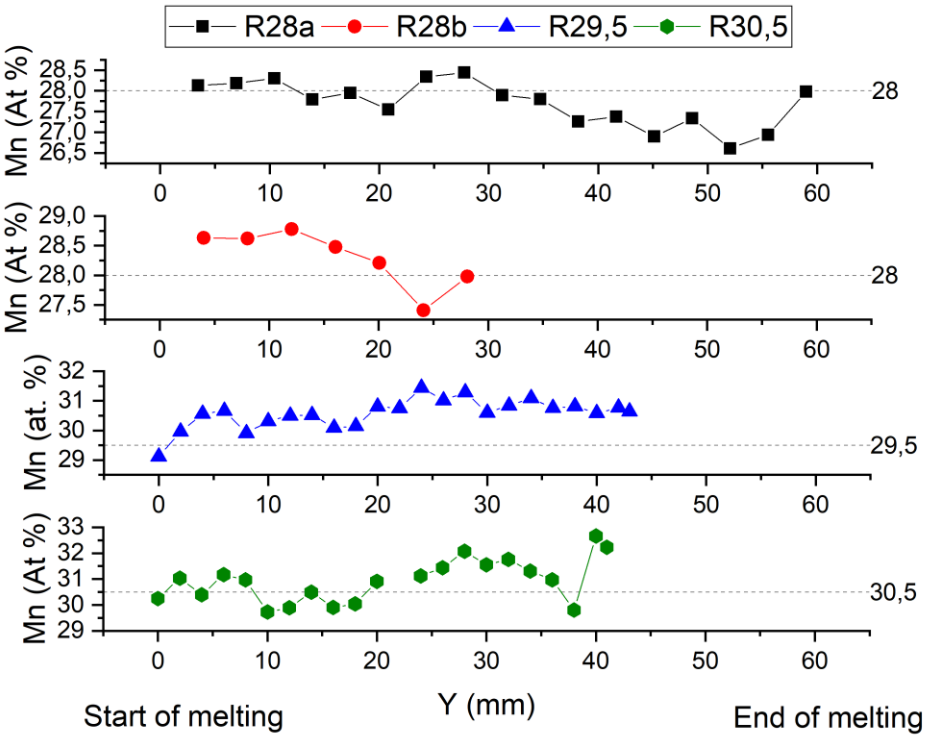

Figure 18 - Manganese composition of all prepared rods along axis of growth, with dashed line representing target composition. Y is the distance from the beginning of the growth.

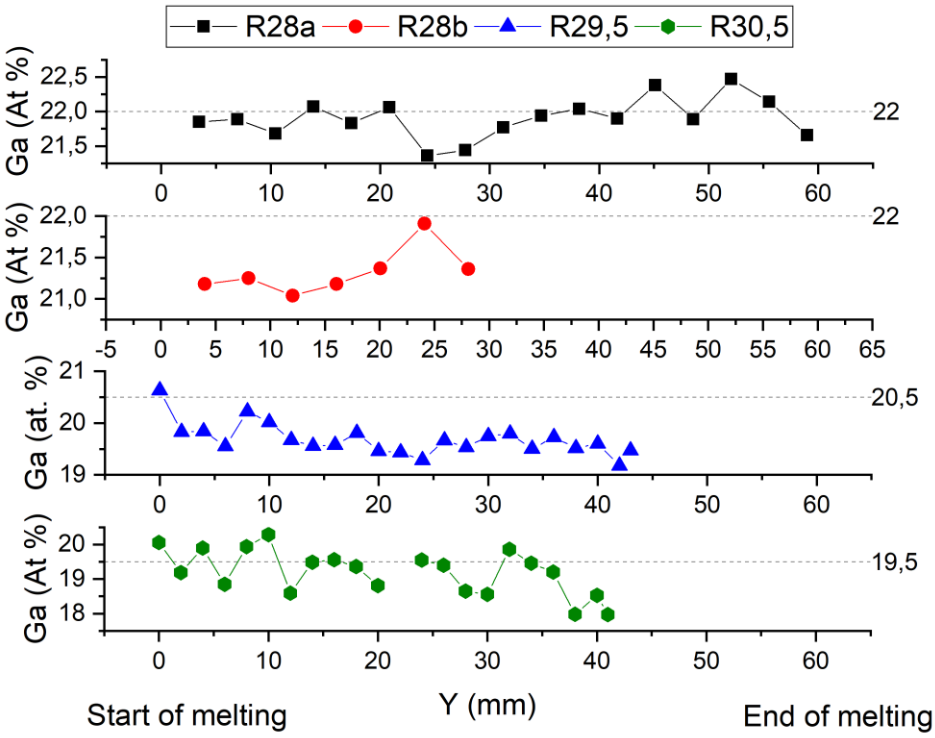

Figure 19 - Gallium composition of all prepared rods along axis of growth, with dashed line representing target composition. Y is the distance from the beginning of the growth.

In Figure 17, Figure 18 and Figure 19 are contents of nickel, manganese and gallium along the rods, respectively. The variation of composition along the rods was within one atomic percent (absolute error). At the end of each rod's growth zone, jump in composition can be observed. This is caused by rapid decrease in lamp output at the end of growth and the fact that molten zone has different composition from the grown crystal, therefore the molten zone solidifies quickly retaining its composition.

The fluctuations of composition can be attributed to failure to uniformly distribute elements in crucible during melting. For example nickel used was in form of small cylinders and gallium was cut from ingot, which means it could not have been mixed like powder and may have contributed to inhomogeneity.

Another cause may be the fact that the diameter of the rod is not uniform along the rod. Because of this, melted volume in floating zone varies and due to that the composition as well. One can see that in the longest rod, a gradient in composition is present, which is somewhat stabilised after approx. 40 mm of growth. Furthermore in R29.5 the gradient in manganese seems to correspond with theoretical model. This is

due to the stabilisation of melt composition explained in chapter 1.1.1. Unfortunately the other samples were not long enough to study this effect.

Despite cleaning the surface face along the rod, it was not completely uniform (oxides), resulting in fluctuating heat transfers in optical furnace along the rod. This leads to uneven evaporation, changes in volume of molten part resulting in variation in composition.

4.1.2. Crystal quality

After the growth in the floating zone furnace, the quality of the crystal was checked. Laue diffraction was performed along the rod, to determine whether the sample is single crystalline or consists of more grains. This was done by measuring at many different points at the rod and comparing diffraction images. In Figure 20 is diffractogram measured during checking for grains in rod R28a along the [111] direction. The arrows point to diffraction which cannot be ascribed to the three fold [111] axis suggesting presence of another grain.

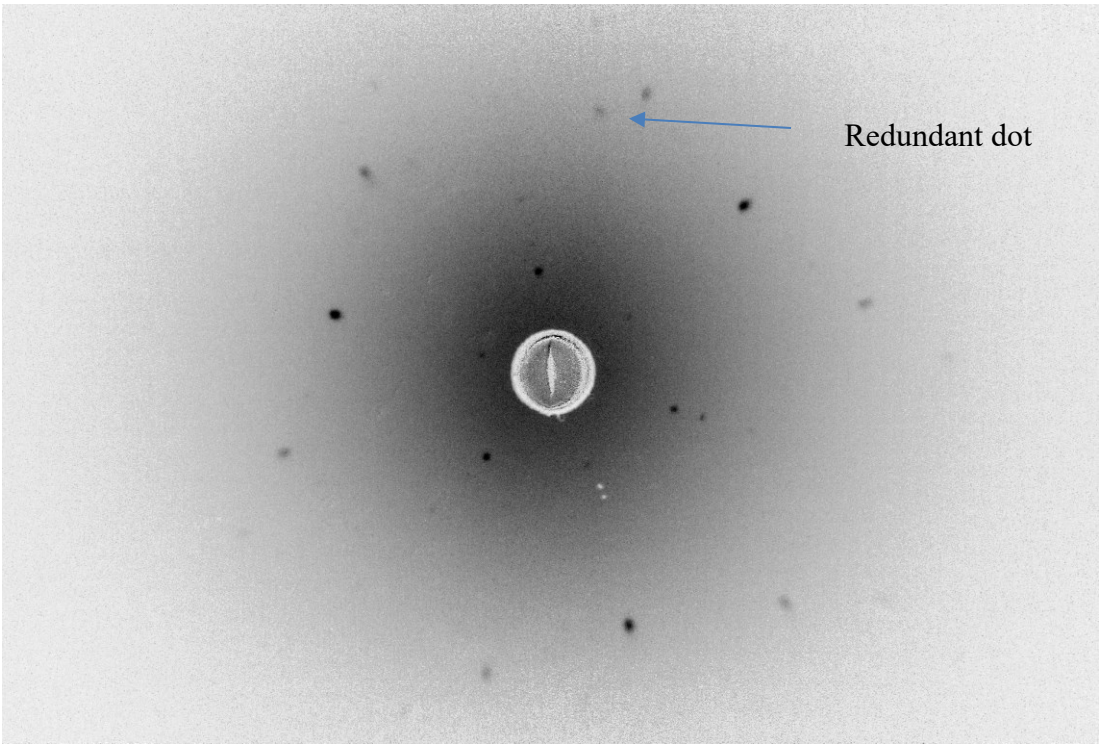

Figure 20 - Diffractogram from part of rod R28 indicating presence of crystal with lesser quality. Dots that do not belong to this symmetry are present, indicating more crystal grains.

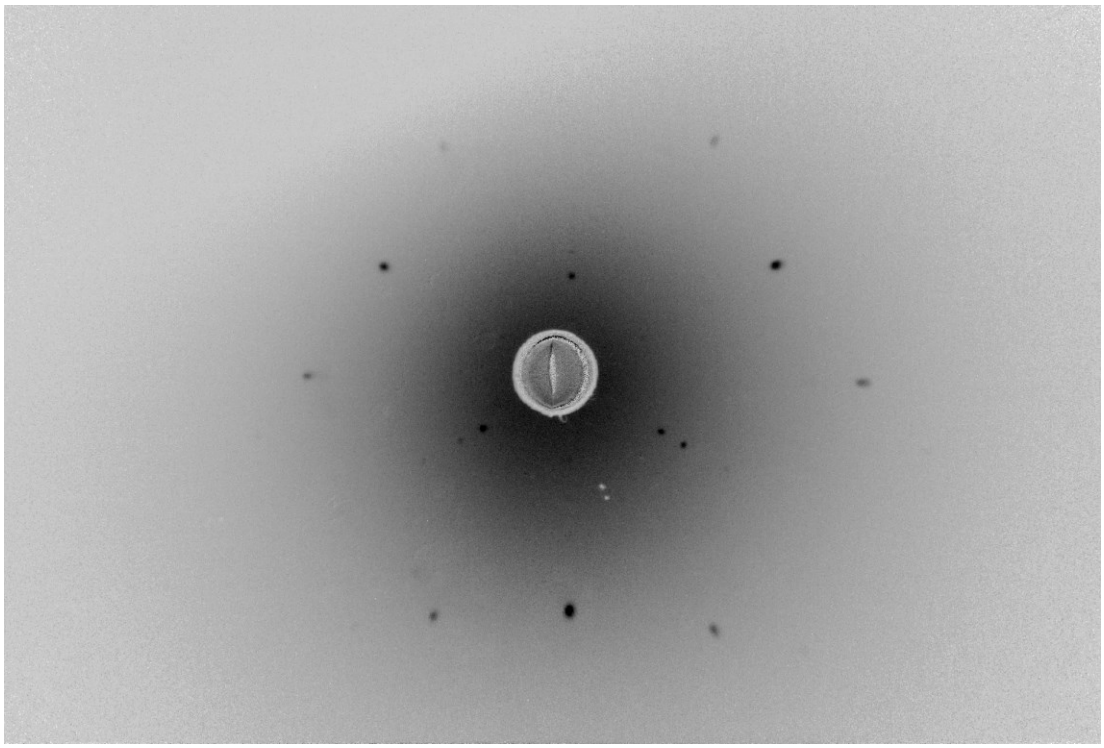

Figure 21- Diffractogram from part of rod R28.5 indicating presence of crystal with higher quality.

In the Figure 21 there is diffractogram taken during grain check of rod R28b. The picture was taken along [111] similarly to previous rod. The rod R28b has sharper picture with no blurred dots and no redundant ones, indicating better crystal quality. Same can be said for more Laue diffractograms taken from R28b. That and the fact that quenching the rod R28b in nitrogen broke it down into three single crystalline pieces of length 2-3 cm whereas no such thing was achieved in R28a, indicates bigger crystals.

Same analysis was done for rods R29.5 and R30.5. The martensitic transition temperature was above room temperature in these two samples. To avoid problem with orienting twinned samples, a heater was attached to the sample holder so the Laue diffraction was performed in the cubic phase (see Figure 22). No big grains were found, furthermore the sections with the same or similar pattern were smaller in R30.5, indicating that much higher than nominal manganese content is causing worse crystals. In spite of that, one good single crystal from rod R29.5 was obtained.

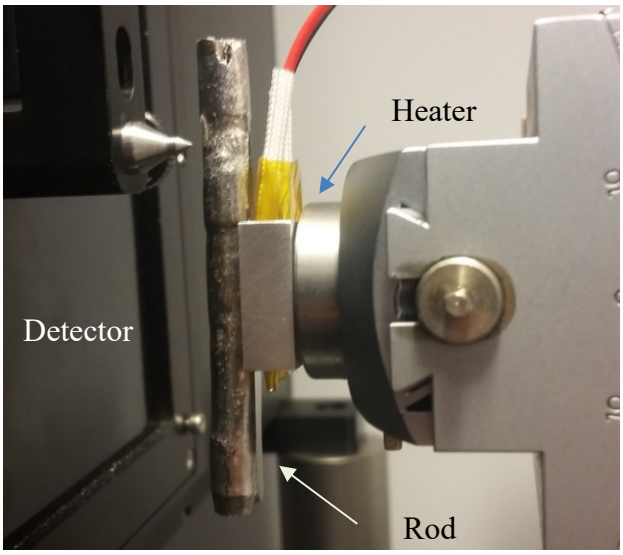

Figure 22 - Rod R29.5 in Laue difractometer, mounted on heating holder, keeping it above transformation temperature.

4.2. Transition temperature identification

Samples for measurements of magnetization, dilatometry and specific heat were cut from prepared rods. They are labelled after their parent rod with additional label (S with a number), for example first sample of R28a was labelled R28a_S1. All samples are listed in Table 2 with their target and actual composition measured via EDS.

Table 2 - List of all samples, their target and actual composition and crystalline structure determined by Laue diffraction.

Name	Target composition	EDS composition	Crystalline structure
R28a_S1	$Ni_{50}Mn_{28}Ga_{22}$	$Ni_{49.97}Mn_{28.16}Ga_{21.87}$	Polycrystalline
R28b_S1	$Ni_{50}Mn_{28}Ga_{22}$	$Ni_{50.40}Mn_{27.90}Ga_{21.70}$	Oriented single crystal
R28b_S2	$Ni_{50}Mn_{28}Ga_{22}$	$Ni_{51.02}Mn_{27.61}Ga_{21.36}$	Single crystal
R28b_S3	$Ni_{50}Mn_{28}Ga_{22}$	$Ni_{50.18}Mn_{28.30}Ga_{21.44}$	Oriented single crystal
R29.5_S1	$Ni_{50}Mn_{29.5}Ga_{20.5}$	$Ni_{49.75}Mn_{30.17}Ga_{20.09}$	Polycrystalline
R29.5_S2	$Ni_{50}Mn_{29.5}Ga_{20.5}$	$Ni_{50.04}Mn_{30.64}Ga_{19.32}$	Oriented single crystal
R30.5_S1	$Ni_{50}Mn_{30.5}Ga_{19.5}$	$Ni_{50.06}Mn_{30.68}Ga_{19.27}$	Polycrystalline
R30.5_S2	$Ni_{50}Mn_{30.5}Ga_{19.5}$	$Ni_{50.45}Mn_{29.84}Ga_{19.71}$	Polycrystalline

4.2.1. Transition identification

The transition temperatures were determined form each type of measurements using methodology explained in Figure 23, 24, 25 and 26. From magnetization

measurements, the transition temperature was determined as can be seen in Figure 23. The data before and after the transition was approximated by lines, the transition temperature was defined as their intersection. Similar method for identifying transitions was used in case of dilatometry measurement (see Figure 24). For DSC measurement the peak wasn't as sharp as in magnetization data however same technique was used. Data was approximated by lines and temperatures are at intercept points. Example can be seen in Figure 25. Martensitic and austenitic transformation are between the same phase, however they have hysteresis, therefore in all graphs distinction between cooling and heating is made via colour (blue for cooling and red for heating). Unfortunately, neither the calorimeter nor the dilatometer has active cooling system, because of that cooling curve down to room temperature was not measured (the measurements stops between 320-340 K) so we cannot detect the transitions on cooling by these two methods.

In following figures μ represents magnetisation of the sample. It is in Bohr magnetons ($\mu_B = \frac{e\hbar}{2m_e}$) per formula unit of the compound, which is unit widely used, when studying microstructure. It is natural unit for expressing magnetic moment of an electron.

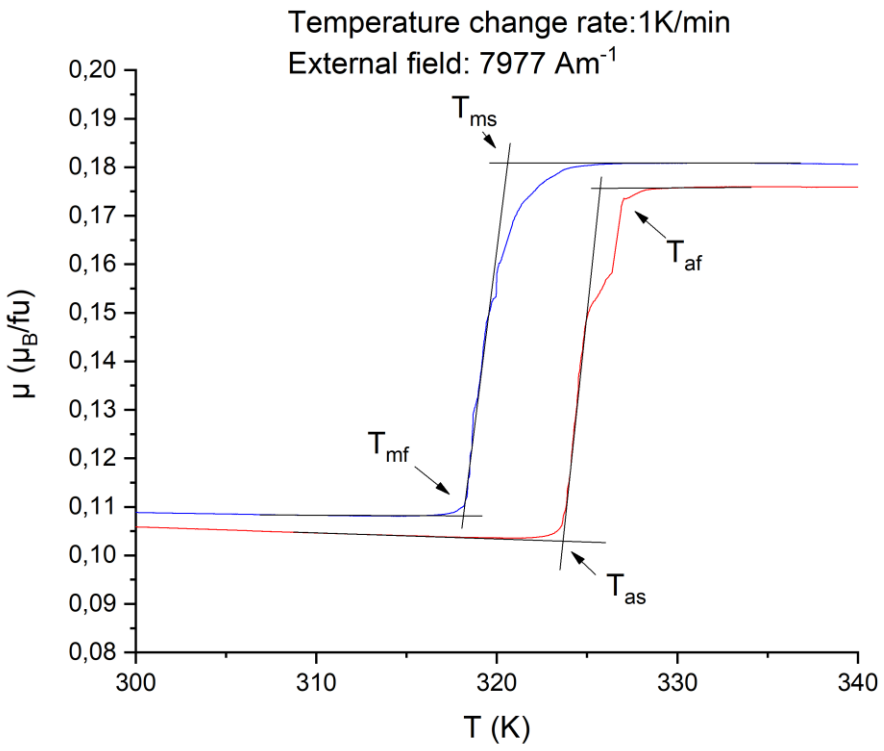

Figure 23 - Magnetization of sample R29.5_S2 showing martensitic and austenitic transition. Identification of start and finish temperature of transitions, where subscripts are "m" for martensitic, "a" for austenitic, "s" and "f" for start and finish respectively. Blue line is cooling and red is heating. Sample oriented along [100].

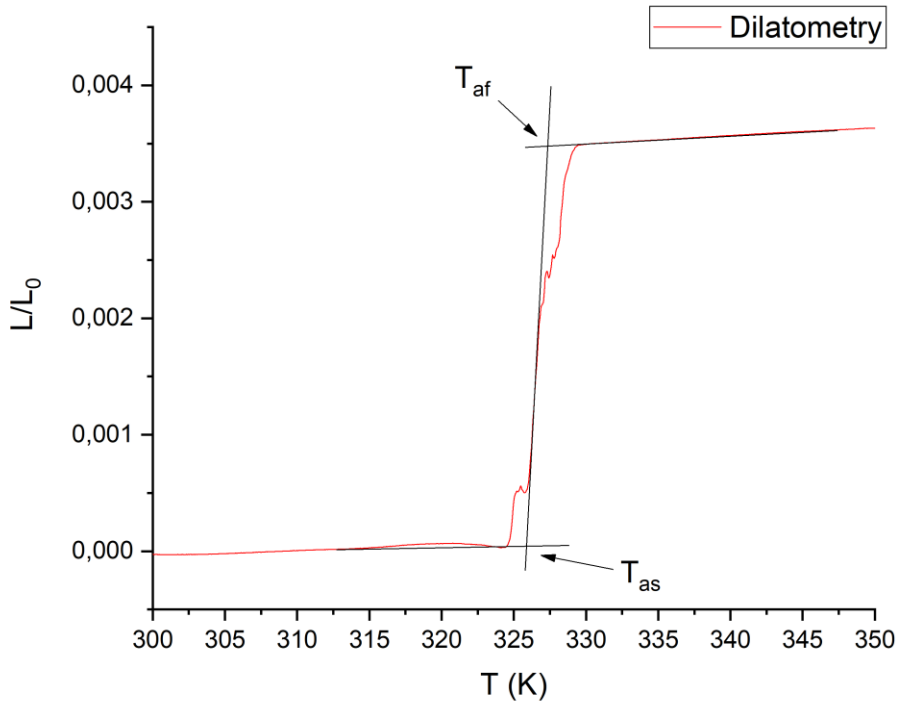

Figure 24 - Deformation of sample R29.5_S2 showing identification of austenitic transition temperature.

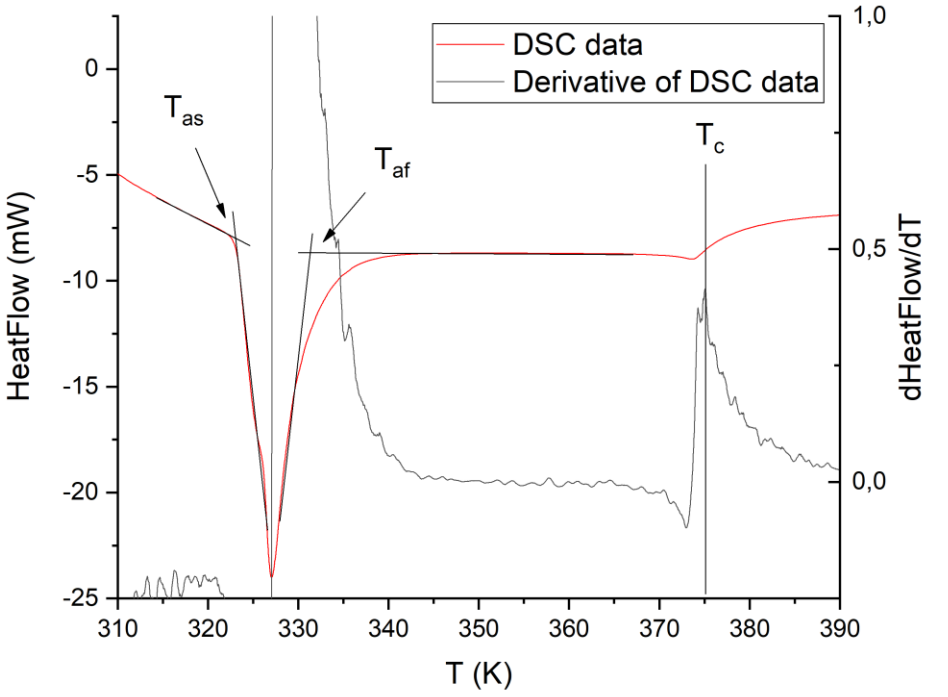

Figure 25 - DSC data for sample R29.5_S2, showing identification of austenitic transition temperatures (heating).

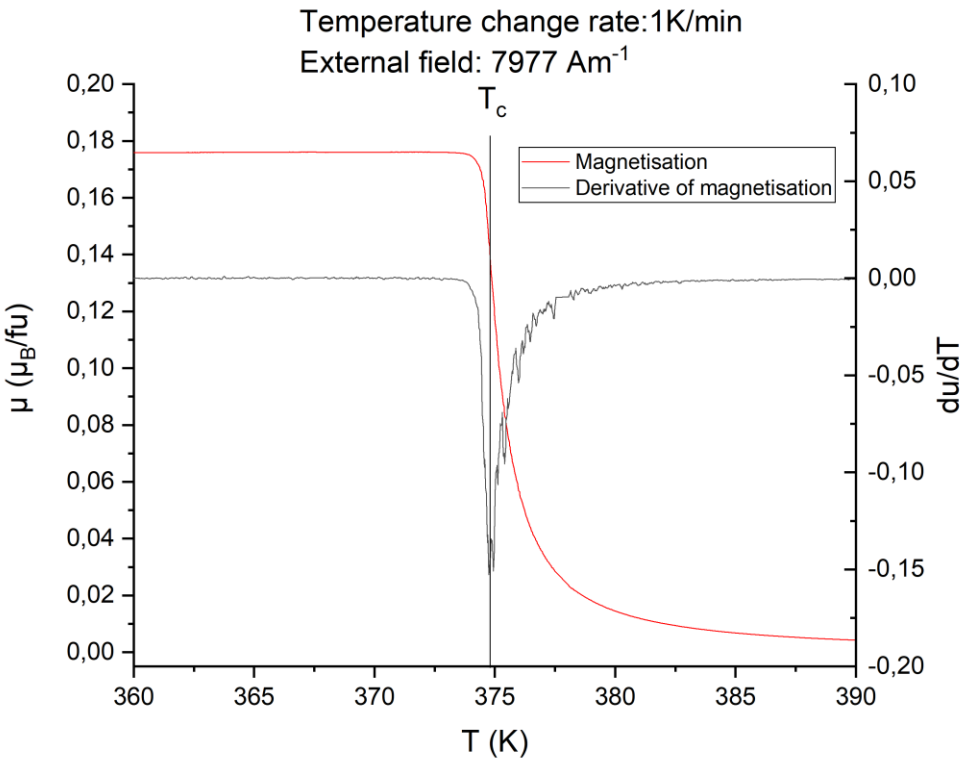

Figure 26 - Curie temperature identification in magnetization data from sample R29.5_S2. Sample oriented along [100].

The transition from paramagnetic to ferromagnetic state is of second order so there is no hysteresis and no latent heat. This was most obvious in the DSC data Figure 25, where only small bump at the Curie temperature was found (compared to the large peak for the structural transition.)From the temperature dependence of magnetization, the Curie temperature was defined as maximum of derivative dM/dT. This can be seen for DSC data in Figure 25. In Figure 23 the Curie temperature is outside range. Example for Curie temperature in magnetization measurement is in Figure 26.

4.2.2. Crystal quality influence on data

In previous subchapter all data shown is from sample R29.5_S2, which was oriented single crystal. All data for R29.5_S2 is in Figure 27. All transitions are sharp and have expected shape. That is because data was measured on single crystal sample R29.5_S2. Even though the magnetization data does show the martensitic transition at approx. 7K higher temperature than DSC and dilatometry, it is still very good agreement. The difference can be due to the fact that the thermometer was not directly attached to the sample and so there could some delay in heating the sample.

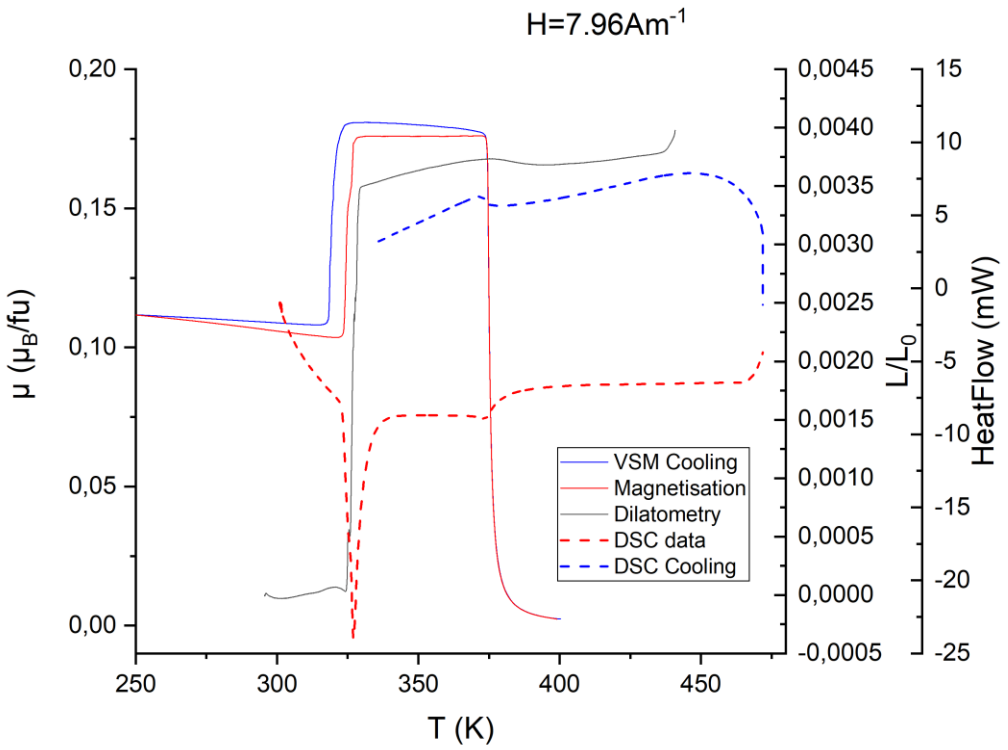

Figure 27 - All measured data for R29.5_S2. Sample oriented along [100].

Not all samples were single crystals, for example R29.5_S1 was polycrystalline. In this sample transition could not be clearly identified, because of this it will not be considered for further examination. Similarly any sample with nickel content differing from target stoichiometry will not be taken into account, because manganese content is studied parameter and comparison data is chosen accordingly, therefore sample R28b_S2 was excluded from further discussion.

4.3. Transition temperature dependence on composition

For comparison of the martensitic and austenitic transitions, we have calculated arithmetic averages of the start and end transformation temperatures introduced above. Instead of Mn concentration a number of valence electrons per atoms is often used in the literature. The Number of valence electrons per atom was calculated based on EDS composition. It was assumed that nickel provides 10, manganese 7 and gallium 3 electrons per atom [23]. The temperature dependence of martensitic transition on the number of electrons per atom is presented in Figure 28. Data has roughly linear dependence as was expected from literature. Similarly in Figure 29 temperature dependence of austenitic transition on electrons per atom is shown, with linear increase as well. For some samples, such as the polycrystalline samples from rod R30.5, different methods (magnetization, DSC, dilatometry) show different transition temperatures, while for single crystals such as sample R29.5_S2 they fairly overlap. The difference between methods may be explained by presence of multiple grains interacting during dilatometry measurement.

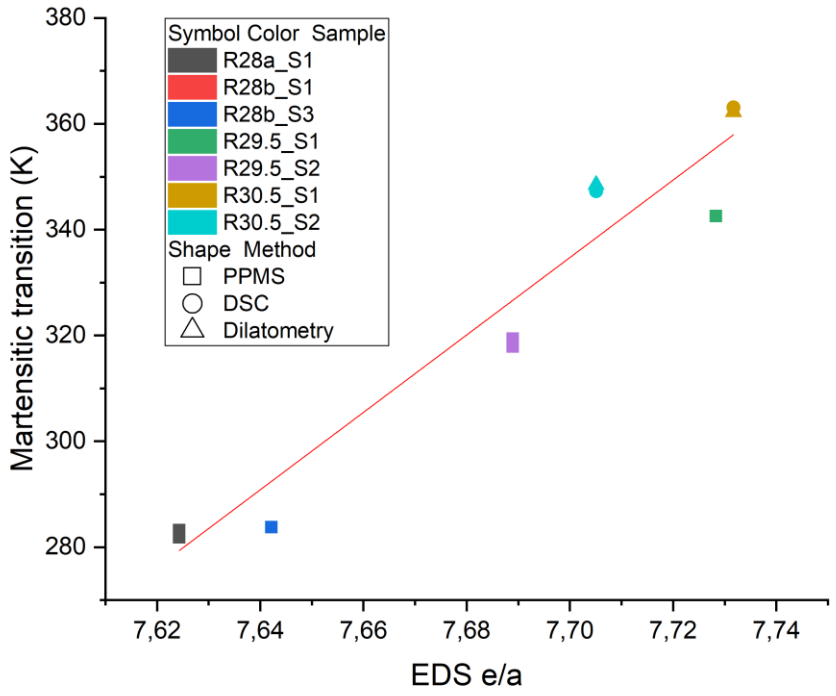

Figure 28 - Dependence of Martensitic transition temperature on electrons per atom in formula unit, colour represents sample and shape method used to measure the transition temperature.

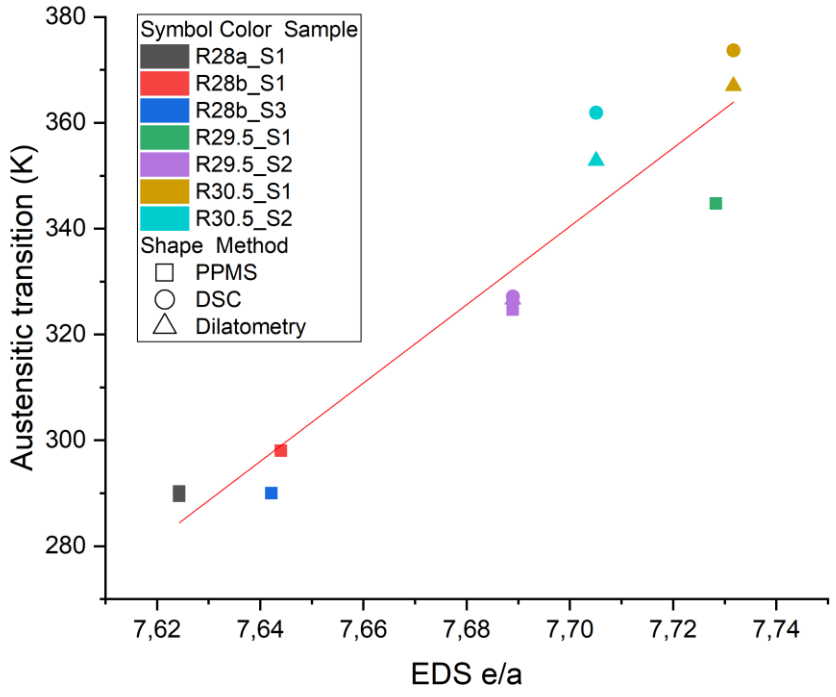

Figure 29 - Dependence of Austenitic transition temperature on electrons per atom in formula unit, colour represents sample and shape method used to measure the transition temperature.

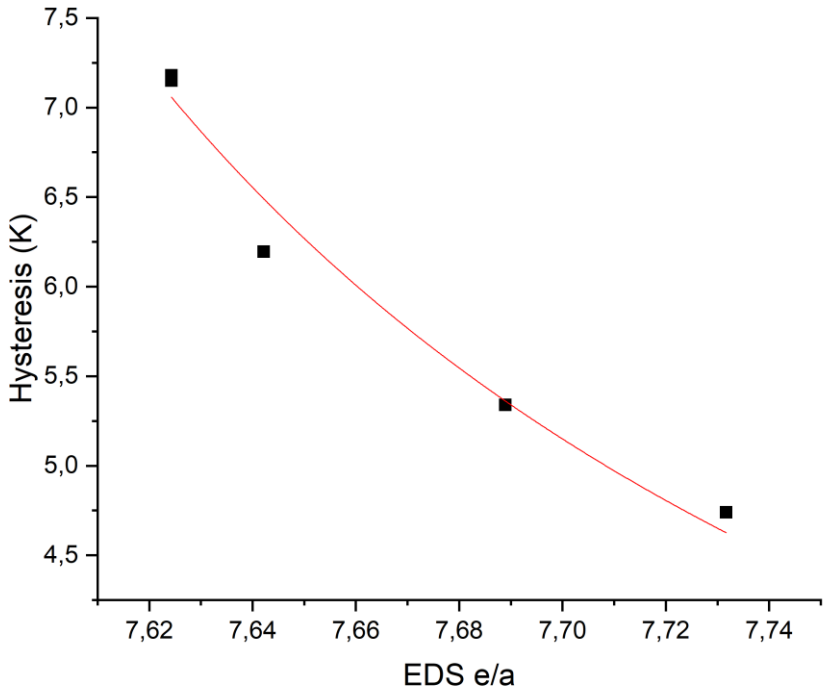

Figure 30 - Width of hysteresis in martensitic/austenitic transition.

With growing e/a the hysteresis between martensitic and austenitic transition temperature decreased roughly as $(e/a)^{-1}$ (see Figure 30). This is beneficial because magnetically induced phase transition is reversible when thermal hysteresis is small, which is desirable in applications.

The Curie temperature dependence on e/a is shown in Figure 31. It has linear trend too. For samples from rod R30.5 no data on Curie temperature is available because the martensitic transition temperature is so high that the peak in DSC data coincides with Curie temperature, therefore it is not visible in the data, the first order type martensitic transition peak is a lot larger (see Figure 25).

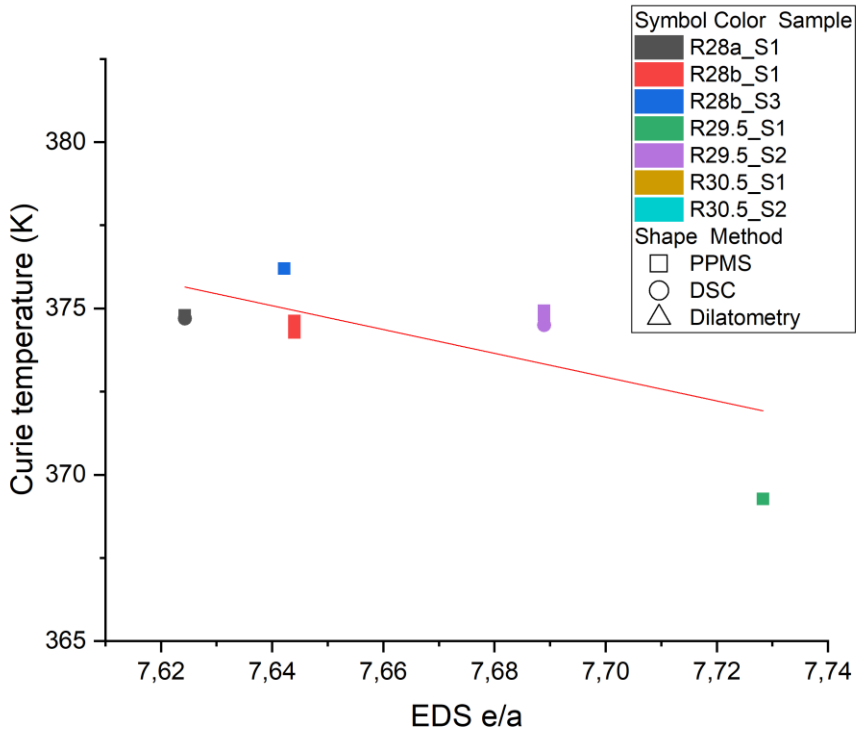

Figure 31 - Curie temperature dependence on number of electrons per atom in formula unit.

The measured transition temperatures were compared to values from literature. Many papers present transition temperatures, but when the composition vs transition temperature dependencies are plotted together the data doesn't seem to show any trend. However, when taking into consideration only papers that checked the composition of grown samples (compared to nominal compositions in the other cases) by EDS or Wavelength-dispersive X-ray spectroscopy (WDS), trend starts to appear. In Figure 32 are all measured martensitic transition temperatures and selected data from literature. It can be seen that transition temperatures determined by our study are is at lower temperatures, nevertheless agrees reasonably with literature. One of the reason can be different calibrations when determining the composition (non-standard EDS in our case). This would mean that all our samples are shifted in the direction of the x axis. In Figure 34 data from this study is shifted -0.01 electron per atom, in this figure data has better match, suggesting that each apparatus has slightly different calibration, the error (0.25 at. %) is within the accuracy of the EDS analysis being ~1%.

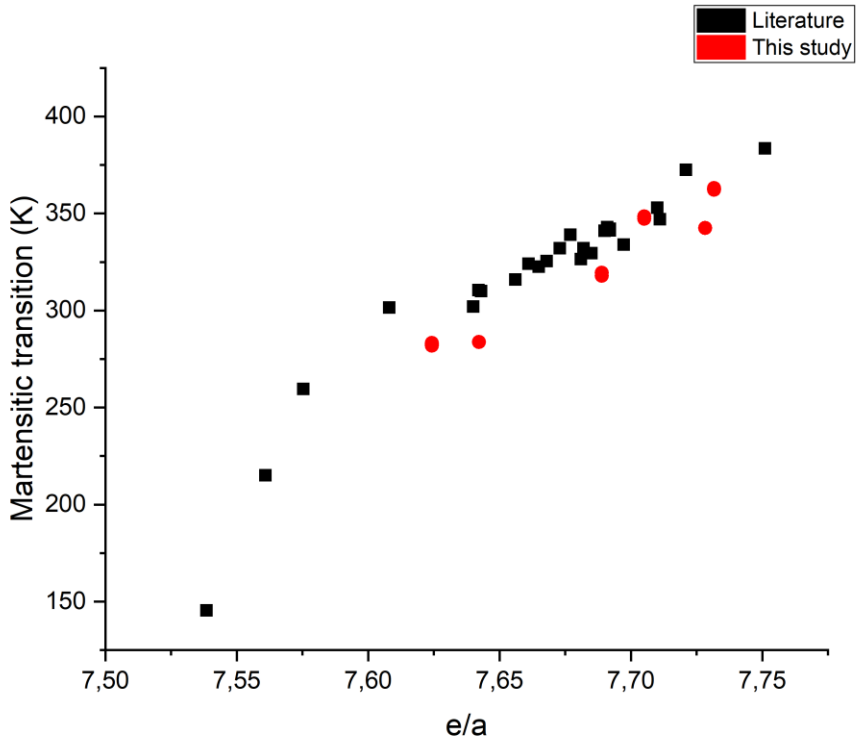

Figure 32 – Martensitic transition temperature dependence on electrons per atom in formula unit. Data extracted from literature and measured on prepared samples.[4, 24–27]

Similar plot for austenitic transition is in Figure 33, this time disagreement between literature and prepared samples is more significant. In this case when data is shifted agreement is better too, further indicating systemic error introduced by EDS (see Figure 35). For smaller number of electrons per atom data from literature is no longer linear, indicating, more complicated dependence. To say for sure however more data in the region around 7.6 e/a is needed.

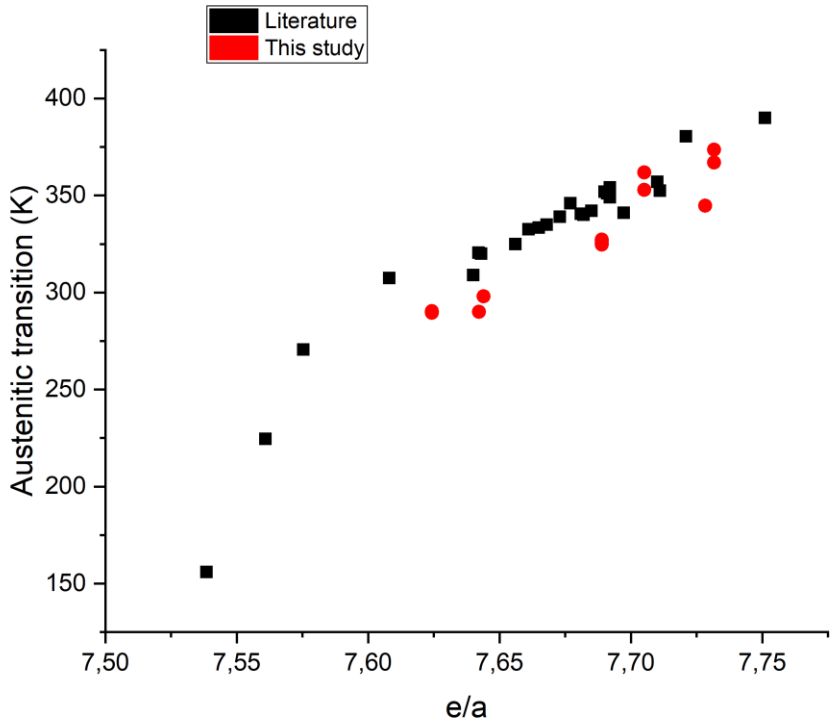

Figure 33 - Austenitic transition temperature dependence on electrons per atom in formula unit. Data extracted from literature and measured on prepared samples.[4, 24–27]

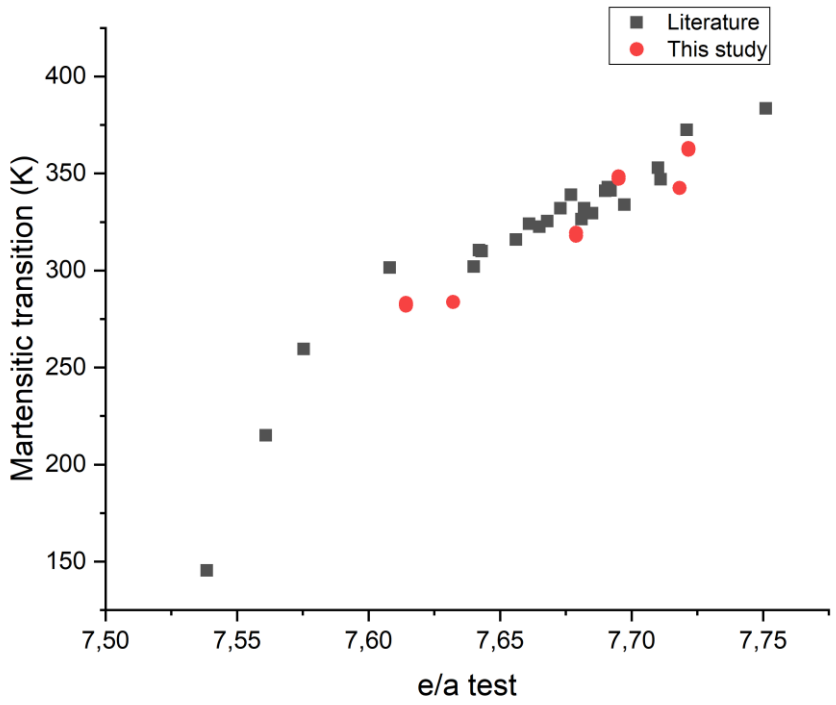

Figure 34 – Martensitic transition temperature dependence on electron per atom in formula unit. Same data as previous figures, but data from this study is shifted -0.01 electrons per atom.

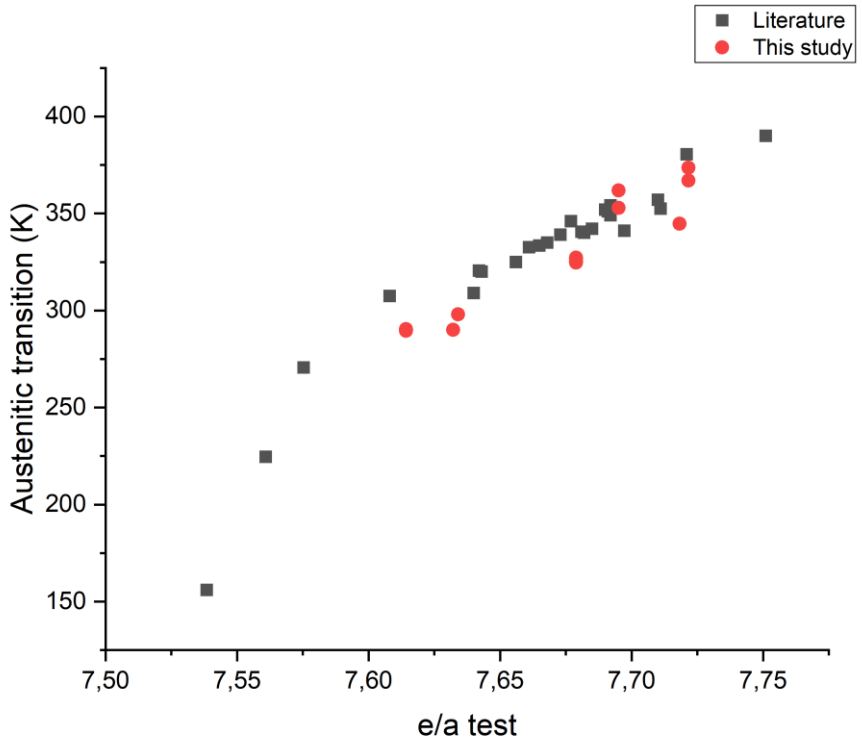

Figure 35 - Austenitic transition temperature dependence on electron per atom in formula unit. Same data as previous figures, but data from this study is shifted -0.01 electrons per atom.

Conclusion

The thesis studies growth of Ni_2MnGa crystal and tuning of its physical properties. Four rods with different compositions were prepared using optical floating zone furnace. The composition variation and crystal quality was studied along the rods. For most rods composition along the rod varies roughly 1 at. %. In rod R29.5 (target composition $Ni_{50}Mn_{29.5}Ga_{20.5}$) composition gradient was observed, as expected based on crystal growth theory. Because of this longer rods should be grown to maximize the stable region. The Crystalline quality of rods was better for rods with lower manganese content, where bigger single crystals were produced.

Samples were taken from rods to measure various physical properties and based on their dependencies on temperature, martensitic/austenitic and para/ferromagnetic transition temperatures were determined. The samples that were in a form of oriented single crystals showed sharp transitions and the temperatures were easily identifiable. On the other hand polycrystalline samples showed less sharp transitions and even multiple transitions, indicating presence of multiple crystal grains with significant variation in composition. We managed to produce single crystal with martensitic transition temperature above room temperature (~320K). For this sample reasonable agreement between measurement techniques was achieved. The measured temperatures were compared with literature. Our data shows similar trend as the literature data, however it seems that it is shifted into lower temperatures. This may have been caused by systemic error introduced by EDS composition measurement.

In order to improve crystal quality single crystalline seed can be used or various precautions to avoid contamination of rods during growth (better holders…) can be taken. Even though we did not attain sufficient homogeneity and crystal quality, this method seems promising and after further tuning will be useful for crystal growth of Ni-Mn-Ga alloys.

Bibliography

1. FELSER, Claudia, WOLLMANN, Lukas, CHADOV, Stanislav, FECHER, Gerhard H. and PARKIN, S. S.P. Basics and prospectives of magnetic Heusler compounds. In : *Springer Series in Materials Science* [online]. AIP Publishing LLC, 2016. p. 37–48. [Accessed 24 March 2019]. ISBN 978-3-319-21448-1. Available from: http://aip.scitation.org/doi/10.1063/1.4917387

2. GRAF, Tanja, CASPER, Frederick, WINTERLIK, Jürgen, BALKE, Benjamin, GERHARD, H, FELSER, Claudia, GRAF, Tanja, CASPER, Frederick, WINTERLIK, Jürgen, BALKE, Benjamin and FECHER, Gerhard H. Crystal Structure of New Heusler Compounds To cite this version : HAL Id : hal-00484131. . 2010.

3. BABITA, Ingale, RAJA, M. Manivel, GOPALAN, R., CHANDRASEKARAN, V. and RAM, S. Phase transformation and magnetic properties in Ni-Mn-Ga Heusler alloys. *Journal of Alloys and Compounds* [online]. 2007. DOI 10.1016/j.jallcom.2006.06.003. Available from: http://www.mendeley.com/research/phase-transformation-magnetic-properties-nimnga-heusler-alloys

4. PAGOUNIS, E., CHULIST, R., SZCZERBA, M.J. and LAUFENBERG, M. High-temperature magnetic shape memory actuation in a Ni–Mn–Ga single crystal. *Scripta Materialia* [online]. 15 July 2014. Vol. 83, p. 29–32. [Accessed 12 May 2019]. DOI 10.1016/J.SCRIPTAMAT.2014.04.001. Available from: https://www.sciencedirect.com/science/article/pii/S1359646214001389

5. PROF. RNDR. VÁCLAV JANIŠ, DrSc. Základní pojmy termodynamiky. . 2019.

6. MASSALSKI, B. Thaddeus. *Binary Alloy Phase Diagrams: Volume 2*. 1990. ISBN 978-0871704030.

7. PAMPLIN, Brian R. *Crystal Growth : International Series on the Science of the Solid State.* Elsevier Science, 2013. ISBN 9781483161464.

8. *ZONE REFINING* [online]. [no date]. [Accessed 14 May 2019]. Available from: http://oscar.iitb.ac.in/OSCARPP/Metallurgical Engineering/UploadedStoryboards/7_Zone refining.pdf

9. HECZKO, O. Magnetic shape memory effect and highly mobile twin boundaries. *Materials Science and Technology*. 2014. Vol. 30, no. 13, p. 1559–1578. DOI 10.1179/1743284714y.0000000599.

10. ROSS HARVEY COLMAN, Dr. *Crystal growth considerations and improvements for better performing Magnetic Shape Memory Alloys (MSMAs)*. 2019.

11. SECHOVSKY, V. Encyclopedia of Materials: Science and Technology : Magnetism in Solids: General Introduction. [online]. 2000. P. 1–15. Available from: http://www.sciencedirect.com/science?_ob=ArticleURL&_udi=&_xRefDocId=pii#b008043152600872x&_user=499885&_fmt=high&_orig=na&_origin=n

a&_cdi=24162&_refWorkId=42&view=c&_acct=C000024500&_version=1&_urlVersion=0&_userid=499885&md5=7b1c9f9a1d63ffa0db8ec24b6715

12. JAROMÍR BROŽ. *Moderní problémy feromagnetismu*. Praha : Nakladatelství Československé akadémie vied, 1962. ISBN 0528-7103.

13. ARORA, Ashima. Optical and electric field control of magnetism. .

14. The Scanning Electron Microscope — Engineering Atoms. [online]. [Accessed 10 May 2019]. Available from: https://www.eng-atoms.msm.cam.ac.uk/RoyalSocDemos/SEM

15. *Využití skenovací elektronové mikroskopie v materiálovém výzkumu* [online]. [no date]. [Accessed 10 May 2019]. Available from: https://physics.mff.cuni.cz/vyuka/zfp/_media/zadani/texty/txt_424.pdf

16. HAFNER, Bob. *Energy Dispersive Spectroscopy on the SEM: A Primer* [online]. [no date]. [Accessed 10 May 2019]. Available from: http://www.charfac.umn.edu/instruments/eds_on_sem_primer.pdf

17. DAVID KŘÍŽ. Úvod do krystalografie a strukturní analýzy. [online]. 2000. [Accessed 10 May 2019]. Available from: http://www.xray.cz/krystalografie/str11c.htm

18. *Lab 31 in TFFM08* [online]. [no date]. [Accessed 10 May 2019]. Available from: http://www.ifm.liu.se/courses/tffm08/dloadsExfys/Lab31_Laue.pdf

19. *Physical Property Measurement System Vibrating Sample Magnetometer (VSM) Option User's Manual* [online]. [no date]. [Accessed 10 May 2019]. Available from: https://web.njit.edu/~tyson/PPMS_Documents/PPMS_Manual/1096-100 Rev. A3 VSM.pdf

20. Dilatometry | Katedra fyziky materiálů MFF UK. [online]. [Accessed 10 May 2019]. Available from: https://material.karlov.mff.cuni.cz/en/equipment/dilatometry

21. *Operating Instructions Sartorius CP|Gem plus Series CPA, GCA and GPA Models Electronic Micro-, Analytical and Precision Balances and Precious Metal Scales* [online]. [no date]. [Accessed 16 May 2019]. Available from: https://www.sartoriusglobal.com/_ui/images/h37/h38/8877021528094.pdf

22. YAN, Yinzhou, SHI, Mengjie, WANG, Qiang and JIANG, Yijian. A simplified finite element model for numerical simulation of temperature field and optimization of parameters in single crystal growth by optical floating zone technique. *Journal of Crystal Growth* [online]. 15 June 2017. Vol. 468, p. 923–932. [Accessed 16 May 2019]. DOI 10.1016/J.JCRYSGRO.2016.09.026. Available from: https://www.sciencedirect.com/science/article/pii/S0022024816305243

23. JIN, X., MARIONI, M., BONO, D., ALLEN, S. M., O'HANDLEY, R. C. and HSU, T. Y. Empirical mapping of Ni-Mn-Ga properties with composition and valence electron concentration. *Journal of Applied Physics*. 2002. Vol. 91, no. 10 I, p. 8222–8224. DOI 10.1063/1.1453943.

24. PAGOUNIS, E., SZCZERBA, M. J., CHULIST, R. and LAUFENBERG, M. Large magnetic field-induced work output in a NiMnGa seven-layered modulated martensite. *Applied Physics Letters*. 2015. DOI 10.1063/1.4933303.

25. SCHLAGEL, D. L., WU, Y. L., ZHANG, W. and LOGRASSO, T. A. Chemical segregation during bulk single crystal preparation of Ni-Mn-Ga ferromagnetic shape memory alloys. *Journal of Alloys and Compounds*. 2000. DOI 10.1016/S0925-8388(00)01161-0.

26. ULLAKKO, K, EZER, Y, SOZINOV, A, KIMMEL, G, YAKOVENKO, P and LINDROOS, V.K. Magnetic-field-induced strains in polycrystalline Ni-Mn-Ga at room temperature. *Scripta Materialia*. 2002. DOI 10.1016/s1359-6462(00)00610-2.

27. ULLAKKO, K., HUANG, J. K., KANTNER, C., O'HANDLEY, R. C. and KOKORIN, V. V. Large magnetic-field-induced strains in Ni2MnGa single crystals. *Applied Physics Letters*. 1996. DOI 10.1063/1.117637.

List of Tables

List of Abbreviations

DSC	Differential scanning calorimetry
BSE	Backscattered electrons
PE	Primary electrons
SE	Secondary electrons
SEM	Scanning electron microscopy
EDS	Energy-dispersive X-ray spectroscopy
PPMS	Physical Property Measurement System
VSM	Vibrating Sample Magnetometer
MPMS	Magnetic Property Measurement System
SQUID	Superconducting Quantum Interference Device
MCE	Magnetocaloric effect
MSM	Magnetic shape memory
MIM	Magnetically induced martensite
MIA	Magnetically induced austenite
MIR	Magnetically induced reorientation